Poroelastic modeling of seismic boundary conditions across a fracture[a)]

Seiji Nakagawa[b)]
Earth Sciences Division, Lawrence Berkeley National Laboratory, 1 Cyclotron Road, Berkeley, California 94720

Michael A. Schoenberg
5 Mountain Road, West Redding, Connecticut 06896

(Received 19 December 2006; revised 15 May 2007; accepted 16 May 2007)

Permeability of a fracture can affect how the fracture interacts with seismic waves. To examine this effect, a simple mathematical model that describes the poroelastic nature of wave-fracture interaction is useful. In this paper, a set of boundary conditions is presented which relate wave-induced particle velocity (or displacement) and stress including fluid pressure across a compliant, fluid-bearing fracture. These conditions are derived by modeling a fracture as a thin porous layer with increased compliance and finite permeability. Assuming a small layer thickness, the boundary conditions can be derived by integrating the governing equations of poroelastic wave propagation. A finite jump in the stress and velocity across a fracture is expressed as a function of the stress and velocity at the boundaries. Further simplification for a thin fracture yields a set of characteristic parameters that control the seismic response of single fractures with a wide range of mechanical and hydraulic properties. These boundary conditions have potential applications in simplifying numerical models such as finite-difference and finite-element methods to compute seismic wave scattering off nonplanar (e.g., curved and intersecting) fractures.
[DOI: 10.1121/1.2747206]

PACS number(s): 43.40.Ph, 43.20.Gp, 43.20.Bi [LLT] Pages: 831–847

I. INTRODUCTION

Rock is often permeated by compliant plane discontinuities (such as fractures and faults) that, depending on their permeability relative to the background, serve as either conduits or barriers to subsurface fluid flow (e.g., Aydin, 1978; Adams and Dart, 1998). In the following, we shall collectively call these discontinuities "fractures." The fluid permeability of a fracture is often a key parameter, yet the quantitative relationship between permeability and its effect on seismic wave scattering is not fully understood. Strong scattering of seismic waves by a fracture is usually related to large permeability, because an open fracture with partial surface contacts has increased mechanical compliance (deformability) (e.g., Pyrak-Nolte and Morris, 2001). However, if a fluid-containing fracture is filled with debris, or a single fracture consists of a large number of microcracks, complex interactions between rock and pore fluid in the fracture result. In this paper, we will develop a simple mathematical model that captures the essential nature of solid-fluid interaction within a fracture, to predict the effect of hydraulic permeability and other fracture properties on seismic wave scattering.

One logical tool for probing the hydrological properties of rocks using seismic waves is Biot's theory of poroelasticity (Biot, 1956a, b), which describes the dynamic interactions of rock and fluid within the pore space. It has been widely recognized, however, that the dispersion and attenuation of seismic waves predicted by the original Biot's theory—which applies to macroscopically homogeneous porous media saturated by a single fluid phase—is often too small to explain the measured velocity dispersion and attenuation of seismic waves. In recent decades, many researchers realized that significant velocity dispersion and velocity attenuation can result at field-relevant frequencies if a rock contains heterogeneity at mesoscale (smaller than seismic wavelength but larger than pore and grain size). One such effect is due to a local fluid-pressure gradient induced at scales comparable to the pressure diffusion length (or, wavelength of Biot's slow compressional waves). These heterogeneities can be, for example, a "patchy" distribution of fluid and gas within rocks (e.g., White, 1975; Dutta and Odé, 1979a, b; and Johnson, 2001) and stratified sedimentary units with different mechanical and hydrological properties (Norris, 1993; Gurevich *et al.*, 1994, 1997; Gelinsky and Shapiro, 1997; Shapiro and Müller, 1999; Pride *et al.*, 2002). A more general theory for heterogeneous poroelastic media, with arbitrary distributions of mechanical and hydraulic properties for both solid and fluid phases, was recently developed by Pride and Berryman (2003a, b).

In general, within porous fluid-bearing rocks, the stronger the fluid permeability and mechanical-property heterogeneity, the more the velocity and attenuation of seismic waves are affected. Fractures are a special case of such heterogeneity, exhibiting an extremely wide range of mechanical com-

[a)]Portions of this work were presented in "Poroelastic modeling of seismic boundary conditions across a fracture," Expanded abstract for the annual meeting for the Society of Exploration Geophysicists, New Orleans, 1–5 Oct. 2006.

[b)]Electronic mail: snakagawa@lbl.gov

pliance and hydraulic permeability (for example, open, air-filled joints to near-rigid, mineral-filled veins), even though they typically occupy only a small volume. Berryman and Wang (1995) examined the mechanical consolidation of media containing a system of compliant high-permeability fractures within a porous background medium, and then used the derived elastic moduli to examine the velocity dispersion and attenuation of low-frequency seismic waves (Berryman and Wang, 2000). The results indicated that the mechanical and hydraulic properties of fractures in a porous host rock affect the behavior of seismic waves. For one-dimensional *P*-wave propagation within a medium containing parallel periodic fractures, Brajanovski *et al.* (2005) derived an analytical model for the dispersion and attenuation of waves. This model was derived by using a wave propagation model for alternating poroelastic layers developed by Norris (1993) and taking the zero-thickness limit of one of the constituting layers to model fractures. Through numerical experiments, attenuation and dispersion of *P* wave propagation was found to be strongly dependent upon the fracture properties (fracture stiffness and density) and the background porosity.

In contrast to previous research, which focused on the velocity and attenuation of waves propagating through materials containing many fractures, in this paper we will develop a simple mathematical model for single poroelastic fractures that can be used to study discrete scattering of seismic waves. The model consists of a set of boundary conditions that relate the stress and displacement (or particle velocity) induced on the fracture surface by passing seismic waves. These boundary conditions are derived using plane-wave theory, by treating a fracture as a thin poroelastic layer with an infinite extent and a small finite thickness. Alternatively, scattering of the plane waves can be examined by using a propagator-matrix method (e.g., Haskell, 1953) and Kennett's reflectivity method (Kennett, 1983) to find an exact relationship between the amplitude of incident and scattered waves. However, the propagator-matrix method suffers an instability when the Biot's slow *P* wave decays too quickly; and Kennett's method results in very complex expressions of the boundary conditions that are not amenable to simple parametrization and interpretation of the consequences for physical acoustics. Further, because both of these methods require knowledge of incident plane waves on both sides of a fracture, they are not well suited to use in other numerical models, such as finite-difference and finite-element methods.

The model developed in this paper provides "jump conditions" that directly relate a wave's particle motions and stress across a fracture without the knowledge of the wave field in the background. Such boundary conditions were initially developed for elastic and viscoelastic fractures, and called the "linear-slip interface model" (Schoenberg, 1980), which led to a plethora of theories and models describing the complex interaction between seismic waves and fractures—e.g., plane-wave scattering theories by Schoenberg (1980), Nakagawa *et al.* (2000), laboratory experiments by Pyrak-Nolte *et al.* (1990), Hsu and Schoenberg (1993), fracture-based anisotropic effective medium theories of Schoenberg and Sayers (1999), Bakulin *et al.* (2000), fracture guided wave studies by Pyrak-Nolte and Cook (1987), and Nihei *et al.* (1999). More recently, Bakulin and Molotkov (1997) developed a similar model for poroelastic fractures, but without including the effect of fracture permeability. These models can be very simple, because when the relative thickness of a fracture is much smaller than the seismic wavelengths (Biot's fast *P* waves and *S* waves), and inertia-related quantities (given as a product of density and fracture thickness) can be ignored, only quasistatic behavior needs to be described (Rokhlin and Wang, 1991). Gurevich *et al.* (1994) also used this fact to derive simple, computationally stable expressions describing the transmission and reflection coefficients of normally incident fast *P* waves for a thin poroelastic layer. Because of its simplicity, the linear-slip model can be used in finite-difference codes to determine the proper effective anisotropic-elastic-moduli values of the numerical grids on a fracture, when the thickness of the fracture is much smaller than the modeling grid spacing (Coates and Schoenberg, 1995).

One important aspect of the linear-slip interface model is that it helps to identify important characteristic parameters of a fracture that control the scattering of seismic waves. An example of such parameters is the fracture compliance. If a fracture is modeled as a mechanically equivalent, thin, compliant layer with a finite thickness, the fracture compliance can be defined as an inverse of the elastic moduli times fracture thickness (e.g., Rokhlin and Wang (1990) defined a fracture stiffness parameter [inverse of the fracture compliance] in this way). Coates and Schoenberg (1995) developed a finite-difference model for fractures and faults, based upon the finite-thickness approximation of fractures and faults. Conversely, when physical properties of a fracture are to be determined using seismic waves, what we can at best determine are these "phenomenological" model parameters (instead of the original material properties and fracture thickness). For a fracture viewed as a thin poroelastic layer, we will show that characteristic parameters similar to the original linear-slip interface model can be defined for a poroelastic fracture, along with other dimensionless parameters that describe its poroelastic properties.

In the following, first we will derive poroelastic seismic boundary conditions (linear-slip interface model) based upon the governing equations of linear, poroelastic wave propagation (Secs. II A and II B). This will result in two sets of independent matrix equations relating displacement and stress across a fracture, which are the primary results of this work. The critical step in this derivation is an approximation of the wave-induced pressure field within a fracture—this is necessary because the exact pressure distribution cannot be determined only from the boundary values. Subsequently, assuming a fracture thickness much smaller than the wavelength of propagating body waves, the derived boundary conditions will be simplified to obtain the characteristic fracture parameters (Sec. II C). The original and simplified boundary conditions will be used to derive explicit expressions for plane-wave transmission and reflection coefficients (Sec. II D). Sections III A and III B will examine the accuracy of the derived boundary conditions (both original and simplified) by comparing the predicted transmission and reflection coefficients to the exact results obtained via Ken-

nett's reflectivity method. Finally, the sensitivity of the transmission and reflection coefficients to the permeability of a fracture will be examined using a characteristic fracture parameter (Sec. III C).

II. THEORY

In this section, we will derive a set of boundary conditions for a thin, isotropic, homogeneous, poroelastic layer embedded within a background medium. (A derivation of boundary conditions assuming a transversely isotropic poroelastic layer for a fracture is also presented in Appendix A.) Subsequently, these boundary conditions are used to derive expressions for transmission and reflection coefficients of incident plane waves within a poroelastic background medium.

A. Governing equations

The governing equations of seismic wave propagation within an isotropic, homogeneous, poroelastic medium can be stated as (e.g., Pride *et al.*, 2002)

$$\boldsymbol{\tau} = G(\nabla \mathbf{u} + \mathbf{u}\nabla) + [(K_U - 2G/3)\nabla \cdot \mathbf{u} + C\nabla \cdot \mathbf{w}]\mathbf{I}, \quad (1)$$

$$-p_f = C\nabla \cdot \mathbf{u} + M\nabla \cdot \mathbf{w}, \quad (2)$$

$$\nabla \cdot \boldsymbol{\tau} = -\omega^2(\rho \mathbf{u} + \rho_f \mathbf{w}), \quad (3)$$

$$-\nabla p_f = -\omega^2(\rho_f \mathbf{u} + \tilde{\rho}\mathbf{w}), \quad \tilde{\rho} \equiv i\eta_f/\omega k(\omega), \quad (4)$$

where $\mathbf{u}$ is the locally averaged, solid-frame displacement vector and $\mathbf{w} \equiv \phi(\mathbf{U}\text{-}\mathbf{u})$ is the fluid-volume displacement vector relative to the solid frame. In this definition of $\mathbf{w}$, $\mathbf{U}$ is the locally averaged (in the pore space) fluid displacement vector and ϕ is the porosity. Equations (1)–(4) assume that the displacement and stress variables depend on $\exp(-i\omega t)$, where ω is the circular frequency. $\mathbf{I}$ indicates an identity tensor, $\boldsymbol{\tau}$ is the total stress tensor, and p_f is the fluid pressure (positive for compression). G is the solid-frame shear modulus, K_U is the undrained bulk modulus, ρ is the bulk density, ρ_f is the fluid modulus, and the parameter $\tilde{\rho}$ is defined in Eq. (4) via fluid viscosity η_f and the frequency-dependent permeability $k(\omega)$ (Johnson *et al.*, 1987). C and M are the Biot's coupling and fluid-storage moduli, respectively. When a plane harmonic wave field is assumed, these equations result in the four plane-wave modes of a Biot medium (fast and slow P waves and two S waves).

Consider an interface across which certain stress and displacement (velocity) components are conserved. We assume this interface to be normal to the 3 direction of Cartesian coordinates, and wave propagation parallel to the 1, 3 plane (Fig. 1). For a homogeneous medium, we can assume a plane harmonic wave field proportional to $\exp i\omega(\xi_1 x_1 - t)$, where ξ_1 is the slowness in the 1 direction. The plane-wave displacement and stress are introduced into Eqs. (1)–(4). Substituting $\partial/\partial x_1 \rightarrow i\omega\xi_1$ and $\partial/\partial x_2 \rightarrow 0$ and eliminating components of the vector and tensor variables w_1, w_2, τ_{11}, τ_{22}, and τ_{12} (which can be discontinuous across the interface), the following two independent sets of coupled first-order differential equations are derived:

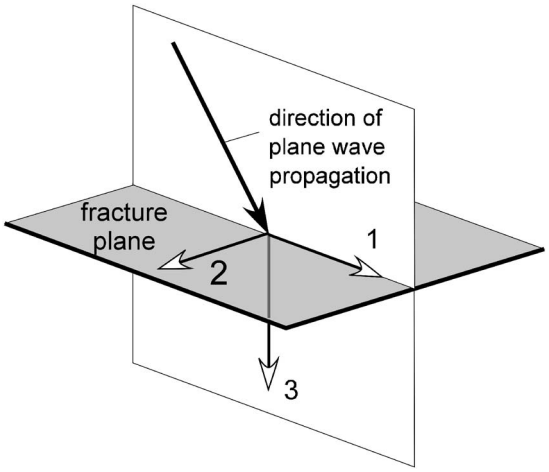

FIG. 1. Cartesian coordinate system used in this paper.

$$\frac{\partial}{\partial x_3}\begin{bmatrix} \dot{u}_2 \\ \tau_{23} \end{bmatrix} = -i\omega \begin{bmatrix} 0 & 1/G \\ -G\xi_1^2 + (\rho\tilde{\rho} - \rho_f^2)/\tilde{\rho} & 0 \end{bmatrix}\begin{bmatrix} \dot{u}_2 \\ \tau_{23} \end{bmatrix} \equiv -i\omega \mathbf{R}\begin{bmatrix} \dot{u}_2 \\ \tau_{23} \end{bmatrix}, \quad (5)$$

$$\frac{\partial}{\partial x_3}\begin{bmatrix} \dot{u}_1 \\ \tau_{33} \\ -p_f \\ \tau_{13} \\ \dot{u}_3 \\ \dot{w}_3 \end{bmatrix} = -i\omega \begin{bmatrix} \mathbf{0} & \mathbf{Q}_{XY} \\ \mathbf{Q}_{YX} & \mathbf{0} \end{bmatrix}\begin{bmatrix} \dot{u}_1 \\ \tau_{33} \\ -p_f \\ \tau_{13} \\ \dot{u}_3 \\ \dot{w}_3 \end{bmatrix}, \quad (6)$$

where

$$\mathbf{Q}_{XY} \equiv \begin{bmatrix} 1/G & \xi_1 & 0 \\ \xi_1 & \rho & \rho_f \\ 0 & \rho_f & \tilde{\rho} \end{bmatrix}, \quad (7)$$

$$\mathbf{Q}_{YX} \equiv \begin{bmatrix} -4G\xi_1^2\left(1 - \frac{G}{H_D}\right) - \frac{\rho_f^2 - \rho\tilde{\rho}}{\tilde{\rho}} & \xi_1\left(1 - \frac{2G}{H_D}\right) & \xi_1\left(-\frac{\rho_f}{\tilde{\rho}} + \alpha\frac{2G}{H_D}\right) \\ \xi_1\left(1 - \frac{2G}{H_D}\right) & \frac{1}{H_D} & -\frac{\alpha}{H_D} \\ \xi_1\left(-\frac{\rho_f}{\tilde{\rho}} + \alpha\frac{2G}{H_D}\right) & -\frac{\alpha}{H_D} & \frac{\alpha^2}{H_D} + \frac{1}{M} - \frac{\xi_1^2}{\tilde{\rho}} \end{bmatrix}. \quad (8)$$

Equation (5) is for wave propagation of S waves with particle motions in the 2 direction, and Eq. (6) is for coupled P (both fast and slow)-S wave propagation with particle motions within the 1,3 plane. Note that both $|\mathbf{R}(\xi_1,\omega)|=0$ and $|\mathbf{Q}_{XY}(\xi_1,\omega)|=0$ yield the dispersion equation for S waves, and $|\mathbf{Q}_{YX}(\xi_1,\omega)|=0$ results in the dispersion equation for fast and slow P waves, where $|\cdot|$ indicates the matrix determinant. The dots over the displacement vector components in Eqs. (5) and (6) indicate that the related quantity is velocity. In Eqs. (7) and (8), $H_D \equiv K_D + 4G/3$ is the dry P-wave modulus and $\alpha=(1-K_D/K_U)/B$ is the Biot-Willis effective stress coefficient (with B as the Skempton coefficient). Using these coefficients, C and M in the governing equations can be expressed as $C=BK_U$ and $M=BK_U/\alpha$. Further, if grains in the porous rock are both isotropic and homogeneous,

$$\alpha = 1 - K_D/K_s, \tag{9}$$

$$B = \frac{1/K_D - 1/K_s}{(1/K_D - 1/K_s) + \phi(1/K_f - 1/K_s)}, \tag{10}$$

where K_D is the dry bulk modulus, K_s is the solid (grain) bulk modulus, K_f is the fluid bulk modulus, and ϕ is the porosity of the medium.

B. Derivation of poroelastic boundary conditions for a fracture

The boundary conditions for a poroelastic fracture are obtained by integrating the governing equations in Eqs. (5) and (6) over a small layer or fracture thickness h as

$$\begin{bmatrix} \dot{u}_2^+ - \dot{u}_2^- \\ \tau_{23}^+ - \tau_{23}^- \end{bmatrix} = -i\omega h \begin{bmatrix} 0 & 1/G \\ -G\xi_1^2 + (\rho\tilde{\rho} - \rho_f^2)/\tilde{\rho} & 0 \end{bmatrix} \begin{bmatrix} \bar{\dot{u}}_2 \\ \bar{\tau}_{23} \end{bmatrix}, \tag{11}$$

$$\begin{bmatrix} \dot{u}_1^+ - \dot{u}_1^- \\ \tau_{33}^+ - \tau_{33}^- \\ -p_f^+ - (-p_f^-) \\ \tau_{13}^+ - \tau_{13}^- \\ \dot{u}_3^+ - \dot{u}_3^- \\ \dot{w}_3^+ - \dot{w}_3^- \end{bmatrix} = -i\omega h \begin{bmatrix} \mathbf{0} & \mathbf{Q}_{XY} \\ \mathbf{Q}_{YX} & \mathbf{0} \end{bmatrix} \begin{bmatrix} \bar{\dot{u}}_1 \\ \bar{\tau}_{33} \\ -\bar{p}_f \\ \bar{\tau}_{13} \\ \bar{\dot{u}}_3 \\ \bar{\dot{w}}_3 \end{bmatrix}, \tag{12}$$

where the superscripts + and − indicate quantities on the boundaries, and the bars above the variables indicate averaged quantities over the thickness of the fracture. At this point, Eqs. (11) and (12) are without approximations, except that we assumed homogeneity of the medium and plane-wave propagation. To derive boundary conditions, the averaged quantities on the right-hand side of the equations have to be expressed exclusively using quantities on the boundaries.

Since the thickness of a fracture h is usually much smaller than seismic wavelengths, the inertial effect and complex multiple scattering of the waves within the fracture can be ignored. This allows us to assume that the solid-frame

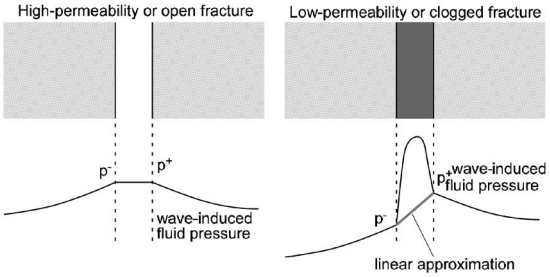

FIG. 2. Cartoon representation of pressure induced by seismic waves for high-permeability (left) and low-permeability (right) fractures. For a high-permeability fracture, fluid pressure on both sides of the fracture can equilibrate during a period of oscillation. In contrast, for a low-permeability fracture, the pressure induced within the fracture may not be able to dissipate. If the pressure field is approximated using a linear function using the boundary values, this can result in a significant error in evaluating the average fluid pressure across the fracture.

velocity and the total stress within the fracture vary smoothly, which can be approximated by a linear function. Also, since the field distribution must be defined by two boundary values on the fracture surfaces, and since there is no knowledge of the field's functional form, a linear function provides the best guess. For Eq. (11), therefore, the boundary condition becomes

$$\begin{bmatrix} \dot{u}_2^+ - \dot{u}_2^- \\ \tau_{23}^+ - \tau_{23}^- \end{bmatrix} = -\frac{i\omega h}{2} \begin{bmatrix} 0 & 1/G \\ -G\xi_1^2 + (\rho\tilde{\rho} - \rho_f^2)/\tilde{\rho} & 0 \end{bmatrix} \times \begin{bmatrix} \dot{u}_2^+ + \dot{u}_2^- \\ \tau_{23}^+ + \tau_{23}^- \end{bmatrix}. \tag{13}$$

In contrast, for Eq. (12), if the permeability of the fracture is low and the fluid within the fracture is not allowed to move freely, excess pore pressure can be induced, which can be very different from the pressure at the interfaces (as illustrated in Fig. 2). This excess pore pressure also induces rapidly changing fluid velocity. Therefore, to provide a better approximation of the spatially averaged fluid pressure and velocity on the right-hand side of Eq. (12), we must examine the behavior of a diffusing fluid pressure field within a low-permeability fracture.

Unfortunately, the quantities on the boundaries alone cannot provide enough information to determine the non-monotoic profile of the field within the fracture. To overcome this difficulty, we first assume that the fluid velocity relative to the frame at the boundaries can be attributed exclusively to slow P waves. This attribution can be justified if $\omega k_0 \rho_f/\eta_f = \rho_f/|\tilde{\rho}(0)| \ll 1$, where $k_0 \equiv k(0)$, because this factor essentially provides the amplitude ratio between the fluid velocity and the solid velocity for fast P waves and S waves. [For example, if a water-filled fracture has a permeability of 10 mD (10^{-14} m^2), $\omega k_0 \rho_f/\eta_f < 0.01$ for frequencies less than 100 kHz.] Therefore, if we define $-p_f^*$ and $\dot{w}_3^*$ as the pressure and fluid flow response excluding the contribution of slow P waves, these are given by an "undrained" fracture (sealed at the boundaries) (Pride, 2003). Note that $-p_f^*$ can be considered uniform across the fracture, due to the long wavelengths of the fast P wave and S wave. Further, we assume that the

spatial average of $\dot{u}_1$ and τ_{33} for this field can be approximated by the average of the total field $\overline{\dot{u}_1}$ and $\bar{\tau}_{33}$. This assumption can be justified if the incident wave is not a slow P wave and the frequency is low, which results in amplitudes of scattered slow P waves much smaller than the sum of the other waves.

Under these assumptions, the jump condition for fluid velocity in the matrix equation [the bottom row of Eq. (12)] can be used to obtain the following relationship:

$$\dot{w}_3^{+*} - \dot{w}_3^{-*} = 0 = -i\omega h\left[\xi_1\left(-\frac{\rho_f}{\tilde{\rho}} + 2\alpha\frac{G}{H_D}\right)\overline{\dot{u}_1} - \frac{\alpha}{H_D}\bar{\tau}_{33} + \left(\frac{\alpha^2}{H_D} + \frac{1}{M} - \frac{\xi_1^2}{\tilde{\rho}}\right)(-p_f^*)\right]. \tag{14}$$

The fluid velocity within the undrained fracture is $\dot{w}_3^*=0$. From the above equation,

$$-p_f^* = \xi_1\frac{\dfrac{\rho_f}{\tilde{\rho}} - 2\alpha\dfrac{G}{H_D}}{\dfrac{\alpha^2}{H_D} + \dfrac{1}{M} - \dfrac{\xi_1^2}{\tilde{\rho}}}\overline{\dot{u}_1} + \frac{\dfrac{\alpha}{H_D}}{\dfrac{\alpha^2}{H_D} + \dfrac{1}{M} - \dfrac{\xi_1^2}{\tilde{\rho}}}\bar{\tau}_{33} \equiv -2G\tilde{B}\tilde{\beta}\xi_1\overline{\dot{u}_1} + \tilde{B}\bar{\tau}_{33}, \tag{15}$$

where we introduced the following coefficients $\tilde{B}$ and $\tilde{\beta}$ for convenience:

$$\frac{1}{\tilde{B}} \equiv \alpha + \frac{H_D}{\alpha M} - \frac{\xi_1^2}{\tilde{\rho}}\frac{H_D}{\alpha} = \frac{H_U}{\alpha M} - \frac{\xi_1^2}{\tilde{\rho}}\frac{H_D}{\alpha}, \tag{16}$$

$$\tilde{\beta} \equiv 1 - \frac{H_D}{2\alpha G}\frac{\rho_f}{\tilde{\rho}}. \tag{17}$$

The first term on the right-hand side of Eq. (15) indicates a contribution of the strain induced in the fracture-parallel direction ($-\xi_1\overline{\dot{u}_1} = \partial\overline{u_1}/\partial x_1$).

Next, we derive an expression for the diffusing pressure and flow field within a fracture using the pressure and velocity at the boundaries and the pressure and velocity for the undrained condition. The solution of diffusing field for slow waves with a slowness ξ_{Ps} is expressed as

$$f(x_3) = A_1 e^{i\omega\xi_{Ps}x_3} + A_2 e^{-i\omega\xi_{Ps}x_3}. \tag{18}$$

We assume that the direction of the diffusion is in the plane-normal direction, which is a reasonable assumption if the velocity of the incoming wave is much faster than the slow P-wave velocity within the fracture. For a set of boundary conditions $f(0)=0$ and $f(h)=1$, the two unknown coefficients are determined, resulting in

$$f(x_3) = \frac{e^{i\omega\xi_{Ps}x_3} - e^{-i\omega\xi_{Ps}x_3}}{e^{i\omega\xi_{Ps}h} - e^{-i\omega\xi_{Ps}h}}. \tag{19}$$

When integrated over an interval $[0, h]$, Eq. (19) becomes

$$\int_0^h f(x_3)dx_3 = \frac{h}{2}\cdot\frac{\tan\omega\xi_{Ps}h/2}{\omega\xi_{Ps}h/2} \equiv \frac{h}{2}\Pi(\varepsilon), \tag{20}$$

where we defined the following dimensionless function:

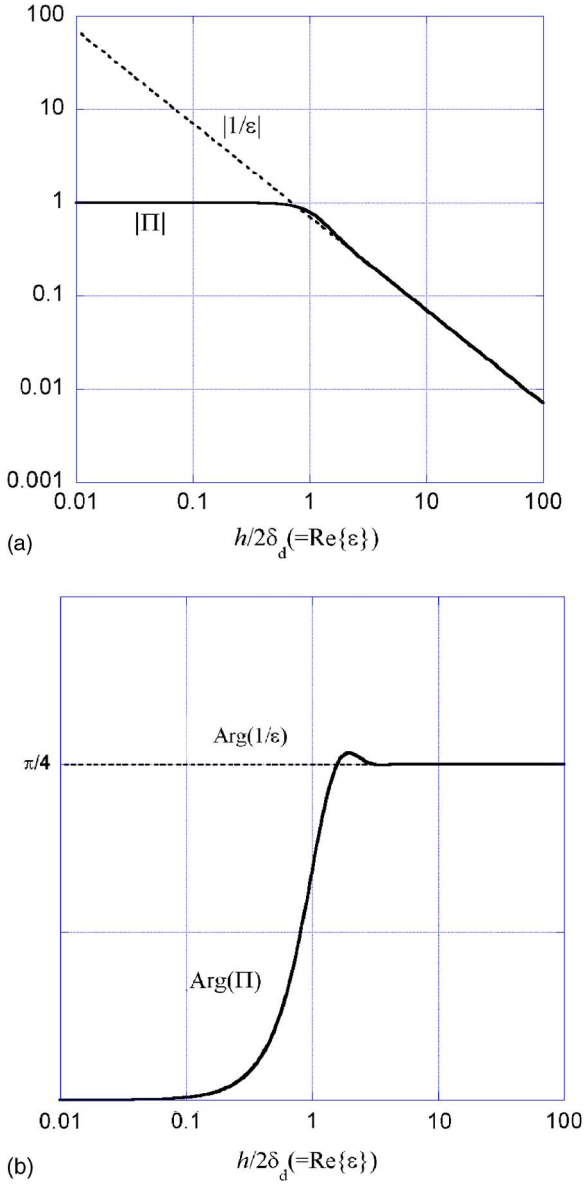

FIG. 3. (Color online) Fluid pressure dissipation factor Π as a function of the dimensionless length parameter $h/2\delta_d$. The behavior of the function changes when the diffusion length is half of the layer thickness, separating the low-frequency drained response (left-hand side of the $h/2\delta_d \sim 1$) and the high-frequency undrained response (right-hand side). (a) Amplitude; (b) Phase (Asymptotes to $\pi/4$ for the undrained response).

$$\Pi(\varepsilon) \equiv \frac{\tanh\varepsilon}{\varepsilon}, \quad \varepsilon \equiv -\frac{i\omega\xi_{Ps}h}{2} = \frac{h}{2\delta_d^*}. \tag{21}$$

The complex fluid-pressure diffusion length δ_d^* is defined through $i\omega\xi_{Ps} \equiv -1/\delta_d^*$. We shall call the dimensionless function Π (Fig. 3) a "fluid-pressure dissipation factor," which approaches unity for the low-frequency limit (drained response) and approaches zero for the high-frequency limit (undrained response). For the aforementioned low frequencies and low-permeability conditions satisfying $\omega\rho_f k_0/\eta_f \ll 1$, the following simple relationship can be used to compute δ_d^* (e.g., Pride, 2003):

$$\frac{1}{\delta_d^*} = \frac{1-i}{\delta_d}, \tag{22}$$

$$\delta_d = \sqrt{\frac{2D}{\omega}}, \tag{23}$$

$$D = \frac{k_0 M}{\eta_f}\left(1 - \frac{C^2}{H_U M}\right) = \frac{k_0 M}{\eta_f}\left(1 - \frac{\alpha^2 M}{H_U}\right), \tag{24}$$

where δ_d is the fluid-pressure diffusion length and D is the fluid-pressure diffusion coefficient. Using the solution for $f(x_3)$, the pressure and fluid velocity within a fracture is given by a superposition having the boundary conditions $-p_f(x_3=0)=-p_f^-$, $-p_f(x_3=h)=-p_f^+$, and $\dot{w}_3(x_3=0)=\dot{w}_3^-$, $\dot{w}_3(x_3=h)=\dot{w}_3^+$. These are

$$p_f(x_3) = p_f^* - (p_f^* - p_f^+)f(x_3) - (p_f^* - p_f^-)f(h - x_3), \tag{25}$$

$$\begin{aligned}\dot{w}_3(x_3) &= \dot{w}_3^* - (\dot{w}_3^* - \dot{w}_3^+)f(x_3) - (\dot{w}_3^* - \dot{w}_3^-)f(h - x_3) \\ &= \dot{w}_3^+ f(x_3) + \dot{w}_3^- f(h - x_3).\end{aligned} \tag{26}$$

As an example, pressure amplitude profiles are shown below in Fig. 4 for assumed boundary values of $-p_f^-=0.25$, $-p_f^+=0.75$, and $-p_f^*=1$. As seen from the plot, the transition between the drained response (linear pressure profile) and the undrained response (constant pressure within the fracture) occurs approximately when $h/2\delta_d=1$, i.e., the sum of the wavelength for the two diffusing pressure waves equals the thickness of the fracture.

Using the result in Eq. (20), pressure and fluid velocity averaged across a fracture is

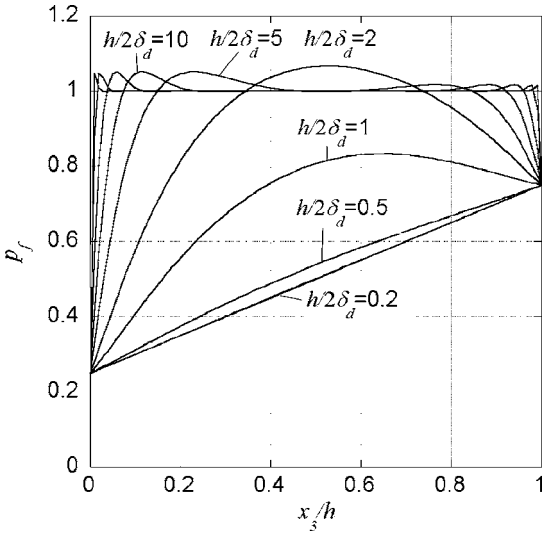

FIG. 4. Amplitude profiles of the pressure field within a fracture for a range of diffusion lengths δ_d. For very large δ_d's (i.e., high frequency, low permeability), the pressure within the fracture can take a value independent from the pressure on the fracture surfaces.

$$\begin{aligned}\bar{p}_f &= \frac{1}{h}\int_0^h p_f(x_3)dx_3 = p_f^* - (2p_f^* - p_f^- - p_f^+)\frac{1}{2}\cdot\Pi(\varepsilon) \\ &= \frac{p_f^- + p_f^+}{2}\cdot\Pi(\varepsilon) + p_f^*\cdot[1 - \Pi(\varepsilon)],\end{aligned} \tag{27}$$

$$\bar{\dot{w}} = \frac{1}{h}\int_0^h \dot{w}_3(x_3)dx_3 = \frac{\dot{w}_3^- + \dot{w}_3^+}{2}\Pi(\varepsilon). \tag{28}$$

Equations (15), (27), and (28) are introduced within the matrix boundary conditions in Eq. (12) to yield

$$\begin{bmatrix} \dot{u}_1^+ - \dot{u}_1^- \\ \tau_{33}^+ - \tau_{33}^- \\ -p_f^+ - (-p_f^-) \\ \tau_{13}^+ - \tau_{13}^- \\ \dot{u}_3^+ - \dot{u}_3^- \\ \dot{w}_3^+ - \dot{w}_3^- \end{bmatrix} = -i\omega h \begin{bmatrix} \mathbf{0} & \mathbf{Q}_{XY} \\ \mathbf{Q}_{YX} & \mathbf{0} \end{bmatrix} \begin{bmatrix} \frac{\dot{u}_1^+ + \dot{u}_1^-}{2} \\ \frac{\tau_{33}^+ + \tau_{33}^-}{2} \\ \frac{-p_f^- + (-p_f^+)}{2}\cdot\Pi + \tilde{B}\left(\frac{\tau_{33}^+ + \tau_{33}^-}{2} - 2G\tilde{\beta}\tilde{\xi}_1\frac{\dot{u}_1^+ + \dot{u}_1^-}{2}\right)\cdot(1-\Pi) \\ \frac{\tau_{13}^+ + \tau_{13}^-}{2} \\ \frac{\dot{u}_3^+ + \dot{u}_3^-}{2} \\ \frac{\dot{w}_3^- + \dot{w}_3^+}{2}\cdot\Pi \end{bmatrix}. \tag{29}$$

The solid displacement (or velocity) u_1, u_3 and total stress τ_{13}, τ_{33} are assumed to vary linearly, because the field changes slowly within the fracture. The above equation is recast in the following form:

$$\begin{bmatrix} \dot{u}_1^+ - \dot{u}_1^- \\ \tau_{33}^+ - \tau_{33}^- \\ -p_f^+ - (-p_f^-) \\ \tau_{13}^+ - \tau_{13}^- \\ \dot{u}_3^+ - \dot{u}_3^- \\ \dot{w}_3^+ - \dot{w}_3^- \end{bmatrix} = -\frac{i\omega h}{2}\begin{bmatrix} \mathbf{0} & \tilde{\mathbf{Q}}_{XY} \\ \tilde{\mathbf{Q}}_{YX} & \mathbf{0} \end{bmatrix}\begin{bmatrix} \dot{u}_1^+ + \dot{u}_1^- \\ \tau_{33}^+ + \tau_{33}^- \\ -p_f^+ + (-p_f^-) \\ \tau_{13}^+ + \tau_{13}^- \\ \dot{u}_3^+ + \dot{u}_3^- \\ \dot{w}_3^+ + \dot{w}_3^- \end{bmatrix}, \tag{30}$$

where

$$\tilde{\mathbf{Q}}_{XY} = \mathbf{Q}_{XY}\begin{bmatrix} 1 & 0 & 0 \\ 0 & 1 & 0 \\ 0 & 0 & \Pi \end{bmatrix} = \begin{bmatrix} 1/G & \xi_1 & 0 \\ \xi_1 & \rho & \rho_f \cdot \Pi \\ 0 & \rho_f & \tilde{\rho} \cdot \Pi \end{bmatrix}, \tag{31}$$

$$\tilde{\mathbf{Q}}_{YX} = \mathbf{Q}_{YX}\begin{bmatrix} 1 & 0 & 0 \\ 0 & 1 & 0 \\ -2G\tilde{B}\tilde{\beta}\xi_1 \cdot (1-\Pi) & \tilde{B} \cdot (1-\Pi) & \Pi \end{bmatrix}. \tag{32}$$

The components of the matrix $\tilde{\mathbf{Q}}_{YX}$ are given explicitly as

$$\tilde{Q}_{YX}(1,1) = -4G\xi_1^2\left(1 - \frac{G}{H_D}\right) - \frac{\rho_f^2 - \rho\tilde{\rho}}{\tilde{\rho}} - 2G\tilde{B}\tilde{\beta}\xi_1^2\left(-\frac{\rho_f}{\tilde{\rho}} + \alpha\frac{2G}{H_D}\right) \cdot (1-\Pi), \tag{33}$$

$$\tilde{Q}_{YX}(1,2) = \xi_1\left[\left(1 - \frac{2G}{H_D}\right) + \left(-\frac{\rho_f}{\tilde{\rho}} + \alpha\frac{2G}{H_D}\right)\tilde{B} \cdot (1-\Pi)\right], \tag{34}$$

$$\tilde{Q}_{YX}(1,3) = \xi_1\left(-\frac{\rho_f}{\tilde{\rho}} + \alpha\frac{2G}{H_D}\right) \cdot \Pi, \tag{35}$$

$$\tilde{Q}_{YX}(2,1) = \xi_1\left(1 - \frac{2G}{H_D} + 2\tilde{B}\tilde{\beta}\alpha\frac{G}{H_D} \cdot (1-\Pi)\right), \tag{36}$$

$$\tilde{Q}_{YX}(2,2) = \frac{1}{H_D} - \alpha\tilde{B}\frac{1}{H_D} \cdot (1-\Pi), \tag{37}$$

$$\tilde{Q}_{YX}(2,3) = -\alpha\frac{1}{H_D} \cdot \Pi, \tag{38}$$

$$\tilde{Q}_{YX}(3,1) = \xi_1\left[-\frac{\rho_f}{\tilde{\rho}} + \alpha\frac{2G}{H_D} - 2\tilde{B}\tilde{\beta}\left(\alpha^2\frac{G}{H_D} + \frac{G}{M} - \frac{\xi_1^2 G}{\tilde{\rho}}\right) \cdot (1-\Pi)\right], \tag{39}$$

$$\tilde{Q}_{YX}(3,2) = -\alpha\frac{1}{H_D} + \left(\alpha^2\frac{1}{H_D} + \frac{1}{M} - \frac{\xi_1^2}{\tilde{\rho}}\right)\tilde{B} \cdot (1-\Pi), \tag{40}$$

$$\tilde{Q}_{YX}(3,3) = \left(\alpha^2\frac{1}{H_D} + \frac{1}{M} - \frac{\xi_1^2}{\tilde{\rho}}\right) \cdot \Pi. \tag{41}$$

Together, Eqs. (13) and (30) are the seismic boundary conditions for a poroelastic fracture.

C. Simplified boundary conditions and characteristic parameters of a fracture

Mathematically, if the components of the matrices in Eqs. (13) and (30) remain finite when the fracture thickness is reduced to zero, the right-hand side of the equations vanishes, and all the variables are continuous across the fracture. However, in reality, a very thin fracture can produce a large discontinuity in displacement and pressure field if viewed as a boundary. For our model to properly capture this behavior, the material properties of a fracture contained in the matrix boundary conditions in Eqs. (13) and (30) have to take values that result in significantly large matrix components, even when multiplied by the small fracture thickness h. To deal with this situation, we can define composite characteristic parameters of a fracture as a combination of the material properties and the fracture thickness, which control the dynamic behavior of the fracture. Conversely, when physical properties of a fracture are to be determined using seismic waves without the knowledge of the fracture thickness, at best we can determine these composite or "phenomenological" parameters instead of the original material properties, such as bulk permeability and elastic moduli.

From Eqs. (13) and (30), following parameters involving fracture thickness h may be defined:

$$\eta_T \equiv \frac{h}{G} \quad \text{(shear compliance)}, \tag{42}$$

$$\eta_{N_D} \equiv \frac{h}{H_D} \quad \text{(dry or drained normal compliance)}, \tag{43}$$

$$\hat{\kappa}(\omega) \equiv \frac{k(\omega)}{h} \quad \text{(membrane permeability)}. \tag{44}$$

If we assume that these parameters are finite for small fracture thicknesses h's, approximate boundary conditions can be obtained by replacing the moduli and permeability in the equations by the parameters and eliminating $O(h)$ terms. For *Sh* waves, this reduces the coefficient matrix in Eq. (13) to

$$h \times \begin{bmatrix} 0 & 1/G \\ -G\xi_1^2 + (\rho\tilde{\rho} - \rho_f^2)/\tilde{\rho} & 0 \end{bmatrix} \to \eta_T\begin{bmatrix} 0 & 1 \\ 0 & 0 \end{bmatrix}. \tag{45}$$

Therefore, the boundary conditions are

$$\begin{cases} \dot{u}_2^+ - \dot{u}_2^- = (-i\omega)\,\eta_T\tau_{23}^- \\ \tau_{23}^+ = \tau_{23}^- \end{cases}, \tag{46}$$

which are exactly the same as the original linear-slip interface model (Schoenberg, 1980).

For the two coupled matrix boundary conditions in Eq. (30) for fast and slow P waves and an S wave, the coefficient matrices $\tilde{\mathbf{Q}}_{XY}$ and $\tilde{\mathbf{Q}}_{XY}$ in Eqs. (31) and (32), multiplied by h, respectively, reduce to

$$h \times \tilde{\mathbf{Q}}_{XY} \rightarrow \begin{bmatrix} \eta_T & 0 & 0 \\ 0 & 0 & 0 \\ 0 & 0 & i\eta_f/\omega\hat{\kappa}(\omega)\cdot\Pi \end{bmatrix}, \tag{47}$$

$$h \times \tilde{\mathbf{Q}}_{YX} \rightarrow \eta_{N_D} \begin{bmatrix} 0 & 0 & 0 \\ 0 & 1-\alpha\tilde{B}(1-\Pi) & -\alpha\cdot\Pi \\ 0 & -\alpha\cdot\Pi & \alpha/\tilde{B}\cdot\Pi \end{bmatrix}, \tag{48}$$

where we used $\tilde{\beta}\approx 1$, which resulted from Eq. (17) through $O(h)\rightarrow 0$. The Skempton coefficient-like parameter in Eq. (16) also reduces to

$$\tilde{B} \approx \alpha\frac{M}{H_U}. \tag{49}$$

Compared to the original Skempton coefficient B, this new coefficient is defined with the undrained P-wave modulus H_U rather than the bulk modulus K_U. Furthermore, the fluid pressure dissipation factor $\Pi(\varepsilon)$ is simplified by approximating the complex diffusion coefficient in Eq. (24) as

$$D \approx \frac{k_0 M}{\eta_f}\left(1-\frac{C^2}{H_U M}\right) = \frac{k_0}{\eta_f}\frac{MH_D}{H_U} = \frac{\tilde{B}\hat{\kappa}_0}{\alpha\eta_f\eta_{N_D}}h^2, \tag{50}$$

which results in

$$\varepsilon = \frac{h}{2\delta_d^*} = \frac{h}{2}(1-i)\sqrt{\frac{\omega}{2D}} = \frac{1-i}{2}\sqrt{\omega\frac{\alpha\eta_f\eta_{N_D}}{2\tilde{B}\hat{\kappa}_0}}. \tag{51}$$

Therefore, for a set of characteristic fracture parameters, $\Pi(\varepsilon)$ also does not depend on the fracture thickness. Note that in deriving Eq. (48), the matrix components in Eqs. (33)–(41) containing $h/\tilde{\rho}=\omega k(\omega)h/i\eta_f$ were ignored, even for fractures with very high (static) permeability. This is because the dynamic permeability of a fracture is finite even when the static permeability of the material within the fracture approaches infinity, which results in an explicit bound $|h/\tilde{\rho}| \le h/\rho_f$ (Appendix B).

Using the simplified relationships in Eqs. (47)–(51), the boundary conditions are written explicitly as

$$\begin{cases} \dot{u}_1^+ - \dot{u}_1^- = (-i\omega)\eta_T\tau_{13}^- \\ \dot{u}_3^+ - \dot{u}_3^- = (-i\omega)\eta_{N_D}\left[\left(1-\alpha\tilde{B}(1-\Pi)\right)\tau_{33}^- - \alpha\dfrac{-p_f^+ + (-p_f^-)}{2}\cdot\Pi\right] \\ \dot{w}_3^+ - \dot{w}_3^- = (-i\omega)\alpha\eta_{N_D}\left[-\tau_{33}^- + \dfrac{1}{\tilde{B}}\dfrac{-p_f^+ + (-p_f^-)}{2}\right]\cdot\Pi \\ \tau_{13}^+ = \tau_{13}^- \\ \tau_{33}^+ = \tau_{33}^- \\ -p_f^+ - (-p_f^-) = \dfrac{\eta_f}{\hat{\kappa}(\omega)}\dfrac{\dot{w}_3^+ + \dot{w}_3^-}{2}\cdot\Pi \end{cases}. \tag{52}$$

An important feature of these boundary conditions is that they do not explicitly contain the plane-parallel slowness ξ_1. This allows us to use Eqs. (46) and (52) for plane waves at any angle of incidence or in the spatial domain of numerical models, such as finite-difference and finite-element models. The last equation for pressure discontinuity in Eq. (52) can be viewed as a generalization of the results from Gurevich and Schoenberg (1999) for Darcy's law extended to a single finite permeability interface. Therefore, from Eqs. (46) and (52), the five fundamental characteristic parameters of a poroelastic fracture are the dry shear and normal fracture compliances η_T, η_{Nd}, membrane permeability $\hat{\kappa}(\omega)$, the fracture Biot-Willis effective stress coefficient α, and the fracture Skempton coefficient $\tilde{B}$. From Eqs. (42) and (43), the dry normal fracture compliance cannot exceed the shear fracture compliance because $H_D=K_D+4G/3\ge G$. This restriction arises because we have assumed that the fracture-filling medium is isotropic. If the layer modeling a fracture is allowed to be transversely isotropic, however, the two compliance parameters can be independent, whereas the same five characteristic parameters of a fracture can be used to describe the boundary conditions in Eqs. (46) and (52) (Appendix A).

The high-permeability limit (open fracture) of Eq. (52) is obtained by taking the limit $\hat{\kappa}_0(\equiv\hat{\kappa}(0))\rightarrow\infty$ ($k_0\rightarrow\infty$ for any h). Using the result $\tilde{\rho}\rightarrow\rho_f$ (Appendix B), $|\eta_f/\hat{\kappa}(\omega)| = |\tilde{\rho}(\omega)|\omega h \rightarrow \rho_f\omega h$, which vanishes for small h's. Because $\Pi\rightarrow 1$, the equations reduce to

$$\begin{cases} \dot{u}_1^+ - \dot{u}_1^- = (-i\omega)\eta_T\tau_{13}^- \\ \dot{u}_3^+ - \dot{u}_3^- = (-i\omega)\eta_{N_D}[\tau_{33}^- - \alpha(-p_f^-)] \\ \dot{w}_3^+ - \dot{w}_3^- = (-i\omega)\alpha\eta_{N_D}[-\tau_{33}^- + (1/\tilde{B})(-p_f^-)] \\ \tau_{13}^+ = \tau_{13}^- \\ \tau_{33}^+ = \tau_{33}^- \\ -p_f^+ = -p_f^- \end{cases}. \tag{53}$$

This is essentially the same result as the boundary conditions derived by Bakulin and Molotkov (1997).

In contrast, the low-permeability limit (impermeable fracture) is obtained by $\hat{\kappa}_0 \to 0$ ($k_0 \to 0$ for any h). Because $\Pi \to O(1/\varepsilon) = O(\sqrt{\hat{\kappa}_0})$ and $1/\hat{\kappa}(\omega) \to 1/\hat{\kappa}_0$, from the third and sixth equations in Eq. (52), $\dot{w}_3^+ - \dot{w}_3^- \to O(\sqrt{\hat{\kappa}_0})$ and $\dot{w}_3^+ + \dot{w}_3^- \to O(\sqrt{\hat{\kappa}_0})$, $\dot{w}_3^+ = \dot{w}_3^- = 0$.As a result, we obtain

$$\begin{cases} \dot{u}_1^+ - \dot{u}_1^- = (-i\omega)\eta_T \tau_{13}^- \\ \dot{u}_3^+ - \dot{u}_3^- = (-i\omega)\eta_{N_U} \tau_{33}^- \\ \dot{w}_3^+ = \dot{w}_3^- = 0 \\ \tau_{13}^+ = \tau_{13}^- \\ \tau_{33}^+ = \tau_{33}^- \end{cases}. \tag{54}$$

In Eq. (54), the undrained normal fracture compliance is defined as a derived new fracture parameter by

$$\eta_{N_U} \equiv \frac{h}{H_U} = \eta_{N_D}(1 - \alpha\tilde{B}). \tag{55}$$

For a compliant, fluid-saturated fracture, $1/\tilde{B} \approx 1/B \approx \alpha$, and Eqs. (53) and (54) can be simplified even further.

Although assuming a vanishingly small fracture thickness h results in simple boundary conditions, in reality a finite h may result in non-negligible effects because of the neglected $O(h)$ terms in the matrices. This error will be examined briefly in the examples given later in Sec. III B.

D. Plane-wave transmission and reflection coefficients

In applying the obtained boundary conditions, we will derive explicit expressions for the transmission and reflection coefficients of plane waves scattered by a poroelastic fracture. From the velocity and stress components used in the equation, Eq. (13) can be used for the scattering of S waves with fracture-parallel particle motions (Sh waves), and Eq. (30) can be used for the scattering of fast and slow P waves, as well as for S waves with particle motions within the plane of wave propagation (Sv waves). In the following, we will first examine the P-Sv case.

First, we split the second matrix boundary conditions in Eq. (30) into the following two coupled equations:

$$\mathbf{b}_X(0_+) - \mathbf{b}_X(0_-) = -i\omega\frac{h}{2}\tilde{\mathbf{Q}}_{XY}(\mathbf{b}_Y(0_+) + \mathbf{b}_Y(0_-)), \tag{56}$$

$$\mathbf{b}_Y(0_+) - \mathbf{b}_Y(0_-) = -i\omega\frac{h}{2}\tilde{\mathbf{Q}}_{YX}(\mathbf{b}_X(0_+) + \mathbf{b}_X(0_-)), \tag{57}$$

$$\mathbf{b}_X \equiv \begin{bmatrix} \dot{u}_1 \\ \tau_{33} \\ -p_f \end{bmatrix}, \tag{58}$$

$$\mathbf{b}_Y \equiv \begin{bmatrix} \tau_{13} \\ \dot{u}_3 \\ \dot{w}_3 \end{bmatrix}, \tag{59}$$

where 0_- indicates the incident side of the fracture and 0_+ is the transmitted side of the fracture. For the matrices $h \times \tilde{\mathbf{Q}}_{XY}$ and $h \times \tilde{\mathbf{Q}}_{YX}$, either the original boundary conditions in Eqs. (31) and (32) or simplified conditions in Eqs. (47) and (48) can be used. The vector variables are decomposed into incident (I), transmitted (T), and reflected (R) fields as

$$\mathbf{b}_X(0_+) = \mathbf{b}_X^T(0_+) = -i\omega\mathbf{X}^+\mathbf{a}^T, \tag{60}$$

$$\mathbf{b}_X(0_-) = \mathbf{b}_X^I(0_-) + \mathbf{b}_X^R(0_-) = -i\omega(\mathbf{X}^+\mathbf{a}^I + \mathbf{X}^-\mathbf{a}^R), \tag{61}$$

$$\mathbf{b}_Y(0_+) = \mathbf{b}_Y^T(0_+) = -i\omega\mathbf{Y}^+\mathbf{a}^T, \tag{62}$$

$$\mathbf{b}_Y(0_-) = \mathbf{b}_Y^I(0_-) + \mathbf{b}_Y^R(0_-) = -i\omega(\mathbf{Y}^+\mathbf{a}^I + \mathbf{Y}^-\mathbf{a}^R). \tag{63}$$

The vectors $\mathbf{b}_{X,Y}^{I,T,R}$ are expressed via coefficient vectors $\mathbf{a}^I$, $\mathbf{a}^T$, and $\mathbf{a}^R$ containing complex amplitudes of solid frame displacement for fast P wave (P_f), slow P wave (P_s), and S wave (S) as their three components (for example, $\mathbf{a}^I = [a_{Pf}^I, a_{Ps}^I, a_S^I]^T$, where the superscript T here indicates vector transpose). The coefficient matrices containing normalized displacement and stress components of these waves in each column are given by

$$\mathbf{X}^{\pm} \equiv \begin{bmatrix} \xi_1/\xi_{Pf} & \xi_1/\xi_{Ps} & \xi_3^S/\xi_S \\ -\xi_{Pf}(H_U^B + f_{Pf}C^B) + 2\xi_1^2 G^B/\xi_{Pf} & -\xi_{Ps}(H_U^B + f_{Ps}C^B) + 2\xi_1^2 G^B/\xi_{Ps} & 2\xi_1\xi_3^S G^B/\xi_S \\ -\xi_{Pf}(C^B + f_{Pf}M^B) & -\xi_{Ps}(C^B + f_{Ps}M^B) & 0 \end{bmatrix} \equiv \mathbf{X} \tag{64}$$

$$\mathbf{Y}^{\pm} \equiv \pm \begin{bmatrix} -2\xi_1\xi_3^{Pf}G^B/\xi_{Pf} & -2\xi_1\xi_3^{Ps}G^B/\xi_{Ps} & -(\xi_S^2 - 2\xi_1^2)G^B/\xi_S \\ \xi_3^{Pf}/\xi_{Pf} & \xi_3^{Ps}/\xi_{Ps} & -\xi_1/\xi_S \\ f_{Pf}\xi_3^{Pf}/\xi_{Pf} & f_{Ps}\xi_3^{Ps}/\xi_{Ps} & -f_S\xi_1/\xi_S \end{bmatrix} \equiv \pm\mathbf{Y} \tag{65}$$

The expressions for the displacement and stress components can be found in, for example, Pride *et al.* (2002). The superscripts + and − indicate waves propagating in the $+x_3$ and $-x_3$ directions, respectively. Arranging displacement and stress components of plane waves as in these matrices has been shown to result in particularly simple expressions for plane-wave transmission and reflection coefficients for materials with "up-down symmetry" across a plane scattering interface (Schoenberg and Protazio, 1992). In the matrices $\mathbf{X}$ and $\mathbf{Y}$, all the slowness components are for the background

TABLE I. Baseline material properties used for the numerical examples are shown. Although some of the values in the table may seem unrealistic for natural fractures, these values are assumed to reduce the number of free parameters in the study.

Matrix properties	Values	Fracture properties	Values
Porosity	0.15	Porosity	0.5
Permeability	1.0×10^{-13} m^2 or 100 mD		
Solid bulk modulus	36.0×10^{9} Pa		
Fluid bulk modulus	2.25×10^{9} Pa		
Frame bulk modulus	9.0×10^{9} Pa	Dry normal compliance	1.0×10^{-11} m/Pa
Frame shear modulus	7.0×10^{9} Pa	Shear compliance	3.0×10^{11} m/Pa
Solid density	2700 kg/m^3	Solid density	2700 kg/m^3
Fluid density	1000 kg/m^3	Fluid density	1000 kg/m^3
Fluid viscosity	1.0×10^{-3} Pa s	Fluid viscosity	1.0×10^{-3} Pa s
Tortuosity	3	Tortuosity	1
Saturation ratio	1		

medium, and coefficients f_{Pf} and f_{Ps} and f_S are the complex-valued ratios of the relative fluid displacement to the solid-frame displacement for fast and slow P waves and the Sv waves, respectively (e.g., Pride *et al.*, 2002). To avoid confusion, moduli for the background medium H_U^B, M^B, and C^B are indicated by a superscript B. Also, all the slowness components are associated with the background medium.

Introducing Eqs. (60)–(65) into Eqs. (56) and (57) results in

$$\mathbf{X}(\mathbf{a}^T-\mathbf{a}^I-\mathbf{a}^R)=-i\omega\frac{h}{2}\tilde{\mathbf{Q}}_{XY}\mathbf{Y}(\mathbf{a}^T+\mathbf{a}^I-\mathbf{a}^R), \tag{66}$$

$$\mathbf{Y}(\mathbf{a}^T-\mathbf{a}^I+\mathbf{a}^R)=-i\omega\frac{h}{2}\tilde{\mathbf{Q}}_{YX}\mathbf{X}(\mathbf{a}^T+\mathbf{a}^I+\mathbf{a}^R). \tag{67}$$

By solving these equations for the unknown coefficient vectors $\mathbf{a}^T$ and $\mathbf{a}^R$, the transmission and reflection coefficient matrices $\mathbf{T}$, $\mathbf{R}$ are determined, respectively, as

$$\mathbf{a}^T=\left[\left(\mathbf{I}+\frac{i\omega h}{2}\mathbf{Y}^{-1}\tilde{\mathbf{Q}}_{YX}\mathbf{X}\right)^{-1}+\left(\mathbf{I}+\frac{i\omega h}{2}\mathbf{X}^{-1}\tilde{\mathbf{Q}}_{XY}\mathbf{Y}\right)^{-1}-\mathbf{I}\right]\mathbf{a}^I\equiv\mathbf{T}\mathbf{a}^I, \tag{68}$$

$$\mathbf{a}^R=\left[\left(\mathbf{I}+\frac{i\omega h}{2}\mathbf{Y}^{-1}\tilde{\mathbf{Q}}_{YX}\mathbf{X}\right)^{-1}-\left(\mathbf{I}+\frac{i\omega h}{2}\mathbf{X}^{-1}\tilde{\mathbf{Q}}_{XY}\mathbf{Y}\right)^{-1}\right]\mathbf{a}^I\equiv\mathbf{R}\mathbf{a}^I. \tag{69}$$

By recognizing the same structure in Eqs. (13) and (30), the same procedure can be followed to determine the scattering coefficients for Sh waves. This can be done by simple substitutions $\mathbf{X}\to1$, $\mathbf{Y}\to-\xi_3^SG^B$, $\tilde{\mathbf{Q}}_{XY}\to1/G$, $\tilde{\mathbf{Q}}_{YX}\to-G\xi_1^2+(\rho\tilde{\rho}-\rho_f^2)/\tilde{\rho}$, $\mathbf{I}\to1$ in Eqs. (68) and (69), resulting, respectively, in

$$a^T=\left[\left(1+\frac{i\omega h}{2}\frac{G\xi_1^2-\rho+\rho_f^2/\tilde{\rho}}{\xi_3^SG^B}\right)^{-1}+\left(1-\frac{i\omega h}{2}\frac{\xi_3^SG^B}{G}\right)^{-1}-1\right]a^I\equiv Ta^I, \tag{70}$$

$$a^R=\left[\left(1+\frac{i\omega h}{2}\frac{G\xi_1^2-\rho+\rho_f^2/\tilde{\rho}}{\xi_3^SG^B}\right)^{-1}-\left(1-\frac{i\omega h}{2}\frac{\xi_3^SG^B}{G}\right)^{-1}\right]a^I\equiv Ra^I. \tag{71}$$

T and R are the transmission and reflection coefficients for Sh waves, respectively.

The general expressions for the transmission and reflection coefficients for poroelastic fractures will be used in the following examples, to examine the accuracy of both the original and simplified boundary conditions.

III. EXAMPLES AND DISCUSSIONS

In this section, we will examine the effects of some of the fracture parameters on seismic wave scattering. The models for the examples share a set of baseline material properties shown in Table I, which are intended to be for a "typical" sandstone (e.g., Berea) containing a compliant fracture. Also, we will focus on the amplitudes of transmitted and reflected fast and slow P waves and an S wave generated by an incident fast P wave. No phase responses are examined.

The accuracy of the derived boundary conditions is assessed by computing the transmission and reflection coefficients using Eqs. (68) and (69) and comparing the results to the prediction of the Kennett's reflectivity algorithm (Kennett, 1983; for poroelastic wave propagation, see Pride *et al.*, 2002). Since the Kennett algorithm computes the scattering coefficients without approximation (Appendix C), the results are considered to be the correct solution.

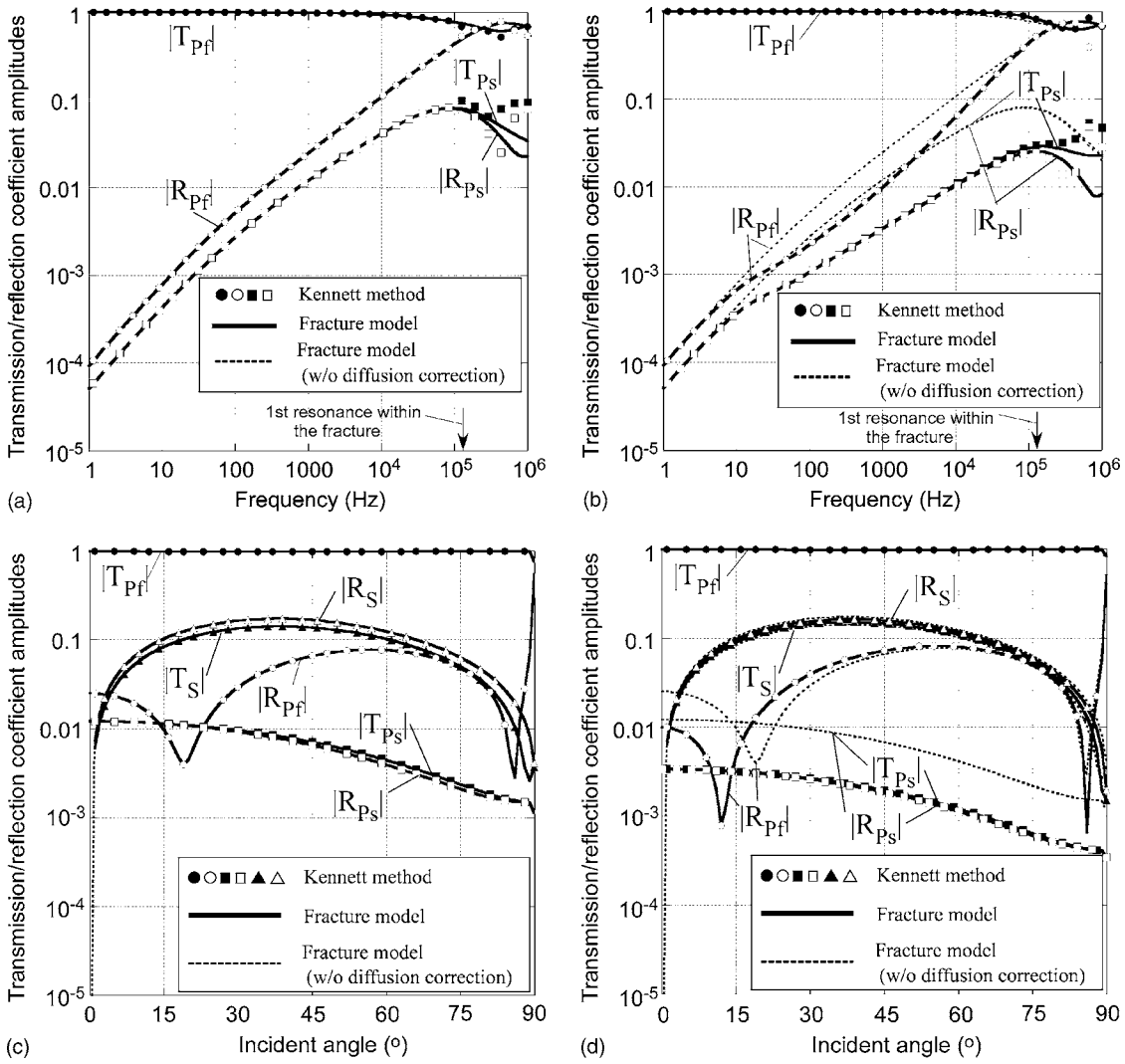

FIG. 5. Amplitudes of the displacement transmission and reflection coefficients for incident fast P waves computed for both low-permeability (1/1000× background) and high-permeability (1000× background) fractures with a thickness $h=1$ mm. The labels indicate T=transmission coefficient and R=reflection coefficient, with subscript Pf=fast P wave, Ps=slow P wave, and $S=S$ wave. (Discrete symbols were computed by the Kennett method.) Solid curves and dotted curves were computed using the full fracture model in Eq. (30) with and without the correction of the pressure diffusion by the fluid pressure dissipation factor Π, respectively. For the high-permeability fracture, the correction is negligible, and both models agree very well with the "correct solution" computed by Kennett method. However, for the low-permeability fracture, the model without the correction shows significant errors. (a) Normal incidence frequency response. $k_0=10^{-10}$ m^2; (b) Normal incidence frequency response. $k_0=10^{-16}$ m^2; (c) 1-kHz angle-of-incidence response. $k_0=10^{-10}$ m^2; (d) 1-kHz angle-of-incidence response. $k_0=10^{-16}$ m^2.

A. Impact of pressure diffusion within a fracture

In the first example, we examine the accuracy of the poroelastic fracture boundary conditions in Eq. (30) and the impact of the fluid pressure dissipation factor Π in Eq. (21) on wave scattering. For this example, in addition to the properties shown in Table I, we assume both high fracture permeability $k_0=10^{-10}$ m^2 (100 D; 1000 times the background permeability) and low fracture permeability $k_0=10^{-16}$ m^2 (0.1 mD; 0.001 times the background permeability), with a fracture thickness $h=1$ mm. The fracture is fully saturated with the same fluid as the background, and the bulk modulus of the solid (grains) is also the same as the background.

Both normal-incidence frequency responses for a frequency range of 10 Hz to 1 MHz—Figs. 5(a) and 5(b)—and angle-of-incidence responses at 1 kHz—Figs. 5(c) and 5(d)—show very good agreement between the Kennett algorithm (shown in discrete symbols) and the full fracture model (shown in thick solid lines). The errors seen above 100 kHz for the normal incidence case result primarily from the multiple scattering of waves within the fracture (layer), which is not accounted for by the fracture model. An approximate frequency corresponding to the lowest-frequency resonance (reverberation) of the fast P wave within the fracture is indicated in the plots by an arrow.

When the effect of pressure diffusion within a fracture is ignored by enforcing the fluid-pressure dissipation factor $\Pi=1$ in Eqs. (30)–(41), the fracture model (shown by dotted lines in Fig. 5) significantly overestimates the reflected fast P wave [Figs. 5(b) and 5(d)] and scattered slow P waves for a low-permeability fracture above a frequency near 10 Hz. This frequency is a transient (critical) frequency that separates the drained and undrained response of a fracture. (More detailed discussion will be given later in Sec. III C.) In con-

trast, for a high-permeability fracture, ignoring the effect of pressure diffusion does not result in noticeable errors [Figs. 5(a) and 5(c)].

B. Fracture thickness and the accuracy of fracture models

We derived the simplified fracture model in Eq. (67) by assuming that the $O(h)$ terms in the original boundary conditions can be ignored except for the characteristic parameters of a fracture. For a finite fracture thickness, however, this assumption has to be scrutinized.

In the following example, we assume a set of characteristic fracture parameters $\eta_T = 3 \times 10^{-11}$ m/Pa, $\eta_{N_D} = 1 \times 10^{-11}$ m/Pa, $\alpha = 0.85$, $\tilde{B} = 0.29$, and $\hat{\kappa}_0 = k_0/h = 1 \times 10^{-13}$ m, and examine the effect of fracture thickness on the wave scattering for three thickness values: $h = 1$ mm, 1 cm, and 10 cm. These characteristic parameters were chosen for the typical physical parameters in Table I, assuming that the 10-cm-thick fracture was 100% saturated by the same fluid as the background. (The bulk modulus of the fluid in the thinner fractures has to be reduced to maintain the same α and $\tilde{B}$ values, which can be realized physically by introducing a small amount of gas in the fluid.) Elastic properties of the material within the fracture are determined from these parameters as a function of fracture thickness and used in the full fracture model in Eqs. (30)–(41) as well as the layer model.

In this example, we also examine the accuracy of the simplified fracture model in Eq. (52) compared to the full fracture model and the layer solution of Kennett's reflectivity algorithm. Reflection and transmission coefficient amplitudes for fast and slow P waves generated from normally incident fast P waves are shown in Fig. 6. For thin fracture thickness h below 1 cm, both full and simplified fracture models agree very well with the layer model, with the upper limit of applicable range of frequency reducing with increasing h. The error becomes large near and above the first resonance frequency of the fast P wave within the fracture, as indicated by a gray vertical line in the plots. The resonance frequencies for this example are lower than the previous example, because the combination of material properties used here yields large undrained fracture compliance, which results in slower fast P-wave velocity within the fracture. Further, for the $h = 10$-cm case, the reflected fast P wave is inaccurately predicted by the simplified model, even well below the resonant frequency. This is probably caused by the effect of mass within the layer. This effect is neglected in the simplified model, since the scattering of slow P waves, which is predominantly governed by the diffusion of fluid pressure within the pore space, is still accurately predicted.

Because the characteristic fracture parameters are not dependent on fracture thickness, the simplified model shows identical responses in Figs. 6(a)–6(c) (shown by thin solid lines). The slight differences in the transmitted slow P-wave response predicted by the model in Fig. 6(c) compared to Figs. 6(a) and 6(b) result from the complex dependence of

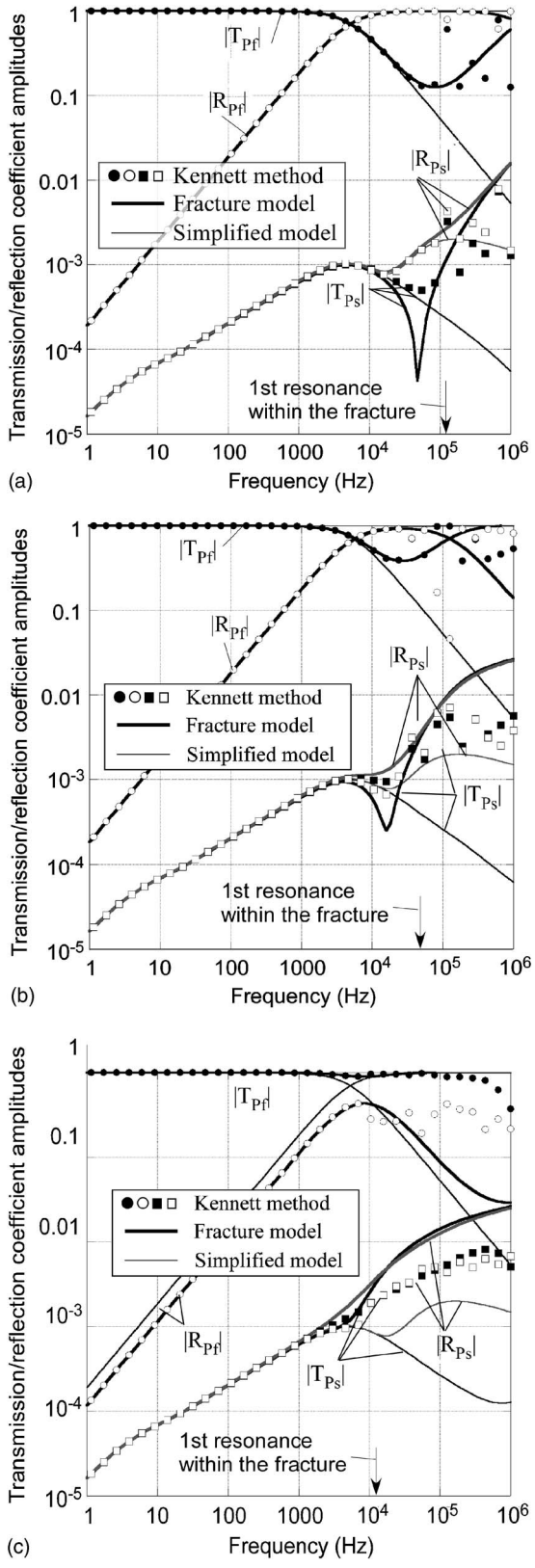

FIG. 6. Normal-incidence reflection and transmission coefficient amplitudes for fast and slow P waves for the same characteristic fracture parameters and three values of fracture thickness. For thin fracture thickness (below 1 cm), both full and simplified fracture models agree very well with the layer model, with the upper limit of the applicable range of frequency reducing with increasing h. For the $h = 10$ cm case, the reflected fast P wave is inaccurately predicted by the simplified model, possibly because of the effect of mass within the layer, which is not considered. (a) $h = 1$ mm; (b) $h = 1$ cm; (c) $h = 10$ cm.

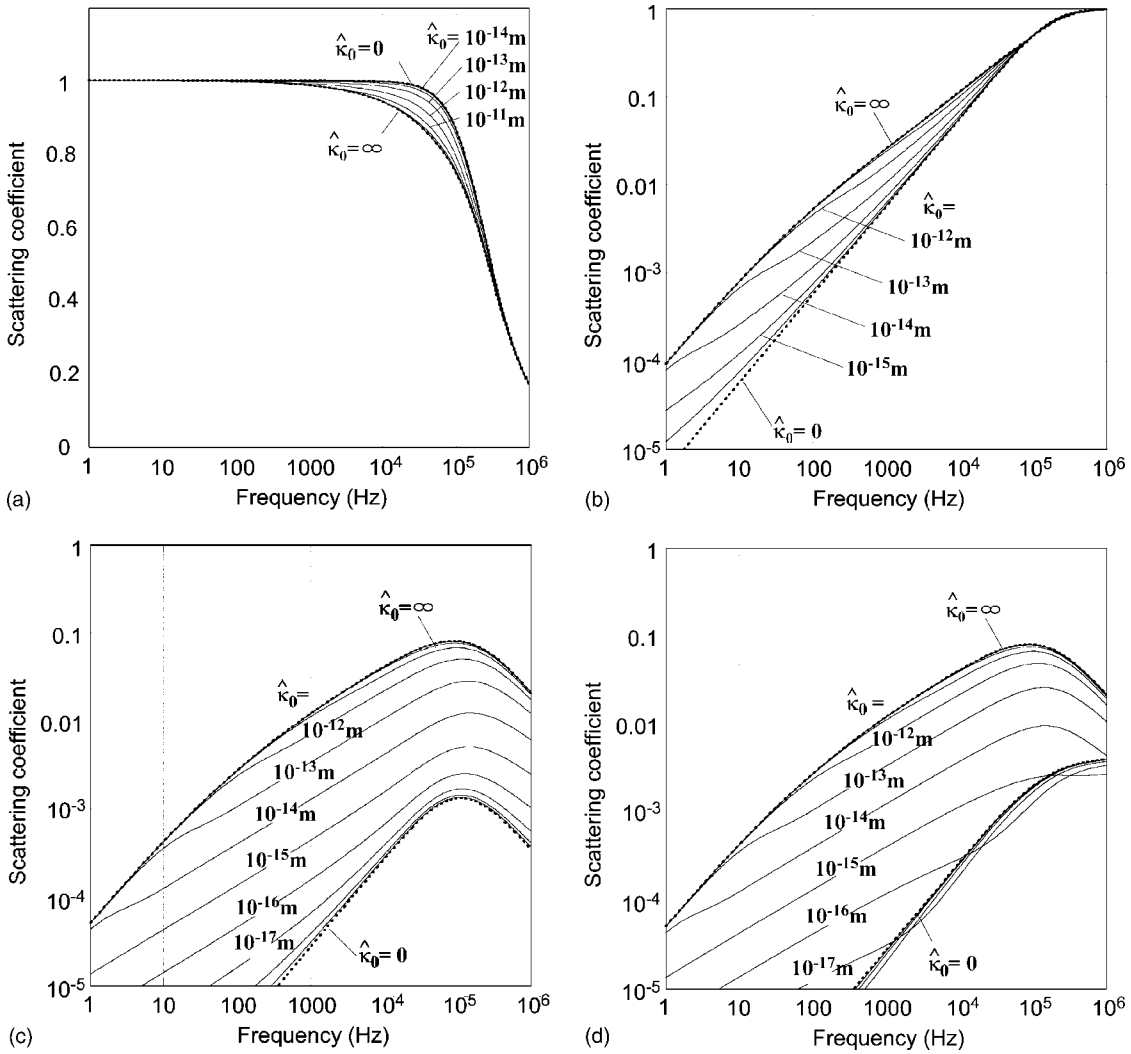

FIG. 7. Scattering amplitude responses (scattering coefficients) for a range of membrane permeability of a fracture. Fast *P*-wave transmission coefficients are shown with semi-log scales to clearly show changes at large amplitudes. Dotted lines are both for a fracture with infinite permeability and an impermeable fracture. Different membrane permeability values correspond to different type curves that "saturate" at both low and high permeability values. (a) Fast *P*-wave transmission; (b) Fast *P*-wave reflection; (c) Slow *P*-wave transmission; (d) Slow *P*-wave reflection.

dynamic permeability on h at high frequencies for a given static membrane permeability [defined by Eq. (44), with a frequency $\omega=0$].

C. Effect of fracture permeability on seismic wave scattering

In the third example, we repeat our experiment of the first example to further examine the effect of fracture hydraulic permeability (or membrane permeability). The material properties and fracture thicknesses used here are the same as in the first example ($h=1$ mm), which results in characteristic fracture parameters $\eta_T=3\times10^{-11}$ m/Pa, $\eta_{N_D}=1\times10^{-11}$ m/Pa, $\alpha=0.998$, and $\tilde{B}=0.98$.

The scattering amplitudes are computed using the simplified fracture model in Eq. (52) for a wide range of membrane permeability values (Fig. 7). To examine the behavior of the waves more closely, each wave and scattering mode is shown separately. We also compute the high-and low-permeability limits of the scattering responses using Eq. (53) and Eq. (54), respectively, which are shown in thick dotted lines bounding finite-permeability responses (except for the zero-permeability bound in the slow *P*-wave reflection in Fig. 7(d), for which the scattering response of a low-permeability fracture is more complicated and undershoots the low-permeability limit).

A distinct characteristic of the reflected fast *P* wave and both transmitted and reflected slow *P* waves is that the slope changes when each frequency response curve departs from that of the high-permeability limit (labeled as $\hat{\kappa}_0=\infty$). For example, for $\hat{\kappa}_0=10^{-13}$ m [corresponding to the case previously shown in Fig. 5(b)], this occurs near 10 Hz. For a saturated fracture with high, dry compliance, this transition (critical) frequency can be evaluated as follows:

From Eq. (51),

$$\varepsilon \approx \frac{1-i}{2}\sqrt{\omega\frac{\alpha^2\eta_f\eta_{N_D}}{2\hat{\kappa}_0\tilde{B}}}. \tag{72}$$

From the behavior of $\Pi(\varepsilon)$ shown in Fig. 3, the transition frequency (critical frequency) ω_d between the drained and undrained responses of a low-permeability fracture is evalu-

ated by a frequency corresponding to $\mathrm{Re}\{\varepsilon\}=1$, resulting in

$$\omega_d = \frac{\hat{\kappa}_0}{\eta_f}\frac{8\tilde{B}}{\alpha^2 \eta_{N_D}}, \tag{73}$$

which is proportional to the membrane permeability of a fracture and inversely proportional to the dry normal compliance of the fracture. When the parameter values used in this example are introduced with $\hat{\kappa}_0 = 10^{-13}$ m, the characteristic frequency is $f_d = \omega_d / 2\pi = 12.7$ Hz, which is close to the 10 Hz observed in both Fig. 5(b) and Figs. 7(b)–7(d). Also, ω_d can be viewed as a critical frequency below which the reflection of fast P waves and the scattering of slow P waves become insensitive to the changes in fracture permeability. Conversely, if the permeability of the fracture is low, for a given frequency, membrane permeability higher than the following critical permeability cannot be determined using seismic waves from the scattering of plane waves,

$$\hat{\kappa}_{0c} = \frac{\omega \eta_f \alpha^2 \eta_{N_D}}{8}. \tag{74}$$

At 1 kHz, the critical membrane permeability is $\hat{\kappa}_{0c} = 7.9 \times 10^{-12}$ m.

IV. CONCLUSIONS

A fluid-filled, flat fracture is a special case of heterogeneous poroelastic media, for which the effect of poroelastic material properties on discrete scattering of seismic waves can be examined analytically, owing to its simple geometry. We hypothesize that a compliant fracture can be viewed as a flat, thin, soft inclusion within a matrix. This simplification results in sets of boundary conditions relating a finite jump in the stress and velocity across a fracture to the stress and velocity at the boundaries (fracture surfaces).

The key step in the derivation of the boundary conditions is the approximation of the pressure field within a fracture: although the thickness of a fracture can usually be considered much smaller than the wavelength of an incoming wave (fast P wave and S wave), the pressure diffusion length (or the wavelength of the generated slow wave) within the fracture can be comparable to the fracture thickness, resulting in a rapid change in the pressure distribution. In turn, this complex pressure distribution due to diffusion affects how the wave is scattered, as a function of permeability and fluid properties within the fracture.

For a thin fracture, however, the permeability parallel to the fracture cannot be resolved from the wave scattering, as indicated by the results in Appendix A. In this case, the permeability needs to be inferred indirectly from the dry and wet fracture compliances—parameters which depend on a fracture's internal structure (such as porosity, asperity, contact spacing), which also affects the permeability. In contrast, fracture-normal permeability can affect wave scattering if the permeability is below a threshold value and the wave frequency is above a critical frequency.

Typically, the scattering behavior of a fracture changes at a frequency where the fluid-solid interaction within the fracture changes between drained (low frequency and high permeability) and undrained (high frequency and low permeability) regimes. In general, for a normally incident fast P wave, a fracture with higher fracture-normal permeability exhibits larger reflection of fast P waves and generates more slow P waves. However, amplitudes of slow P waves generated by a single fracture are generally small. For the effect to be clearly measurable, high-frequency seismic waves and/or multiple fractures may be necessary.

The scattering of waves by a fracture is controlled by a set of characteristic (phenomenological) parameters similar to the fracture compliance used in the linear slip interface model (Schoenberg, 1980). These parameters are shear compliance, drained normal compliance, Biot-Willis effective stress coefficient, fracture Skempton coefficient, and membrane permeability. For a sufficiently small fracture thickness, fractures having identical parameter values result in the same observed seismic response.

Finally, throughout the modeling presented in this paper, a fracture is assumed to be an isotropic and homogeneous layer. (An extension of the model to anisotropic elastic moduli and permeability is presented in Appendix A.) The question remains, can an open fracture with partial surface contacts and a fault with complex internal geometry be modeled with such a simple model? For example, scattering of waves may be strongly affected by the local fluid motion around contacting asperities and within the complex internal structure of a well-developed fault originating from shearing (e.g., Sibson, 1977). For such cases, more complex boundary conditions, considering the effect of internal heterogeneity of a fracture, are necessary.

ACKNOWLEDGMENTS

This research has been supported by the Office of Science, Office of Basic Energy Sciences, Division of Chemical Sciences of the U.S. Department of Energy under Contract No. DE-AC76SF00098. The authors would like to thank Dr. Steven Pride at Lawrence Berkeley National Laboratory for many useful suggestions and discussions during the development of the models presented in this article.

APPENDIX A: DERIVATION OF SEISMIC BOUNDARY CONDITIONS FOR A TRANSVERSELY ISOTROPIC POROELASTIC FRACTURE

Constitutive relationships for a general anisotropic poroelastic medium can be written using index notations as (Cheng, 1997)

$$\tau_{ij} = C^D_{ijkl} u_{k,l} + \alpha_{ij}(-p_f) = C^U_{ijkl} u_{k,l} + M \alpha_{ij} w_{k,k}, \tag{A1}$$

$$-p_f = M(w_{k,k} + \alpha_{ij} u_{i,j}), \tag{A2}$$

where α_{ij} is the symmetric Biot-Willis effective stress coefficient tensor and C^D_{ijkl} and $C^U_{ijkl} = C^D_{ijkl} + M\alpha_{ij}\alpha_{kl}$ are the dry (drained) and undrained stiffness tensors for the solid frame, respectively. M is the fluid storage modulus. The momentum balance equations are

$$\tau_{ij,j} = -\omega^2(\rho u_i + \rho_f w_i), \tag{A3}$$

$$-p_{f,i} = -\omega^2(\rho_f u_i + \tilde{\rho}_{ij} w_j), \tag{A4}$$

where $\tilde{\rho}_{ij}$ is defined via an anisotropic dynamic permeability tensor $\mathbf{k}(\omega)$ through $\tilde{\boldsymbol{\rho}} \equiv (i\eta_f/\omega)\mathbf{k}^{-1}(\omega)$.

For the following, we will focus on the transversely isotropic case with the axis of symmetry aligned in the 3 direction (fracture-normal direction). In the reduced matrix notation, the above constitutive relationship becomes

$$\begin{bmatrix} \tau_{11} \\ \tau_{22} \\ \tau_{33} \\ \tau_{23} \\ \tau_{31} \\ \tau_{12} \end{bmatrix} = \begin{bmatrix} C_{11}^D & C_{12}^D & C_{13}^D & & & \\ C_{12}^D & C_{11}^D & C_{13}^D & & & \\ C_{13}^D & C_{13}^D & C_{33}^D & & & \\ & & & G & & \\ & & & & G & \\ & & & & & G' \end{bmatrix} \begin{bmatrix} u_{1,1} \\ u_{2,2} \\ u_{3,3} \\ u_{2,3} + u_{3,2} \\ u_{3,1} + u_{1,3} \\ u_{1,2} + u_{2,1} \end{bmatrix} + \begin{bmatrix} \alpha_1 \\ \alpha_1 \\ \alpha_3 \\ 0 \\ 0 \\ 0 \end{bmatrix} (-p_f), \tag{A5}$$

$$-p_f = M(\alpha_1 u_{1,1} + \alpha_1 u_{2,2} + \alpha_3 u_{3,3}) + M(w_{1,1} + w_{2,2} + w_{3,3}), \tag{A6}$$

where $G' = (C_{11}^D - C_{12}^D)/2$, and α_i $(i=1, 3)$ are the diagonal entries of the effective stress coefficient tensor α. The momentum balance equation is the same as the general anisotropic case, except that the permeability tensor also becomes diagonal: $\mathbf{k}(\omega) = \mathrm{diag}[k_1(\omega), k_1(\omega), k_3(\omega)]$, where each diagonal component can be computed using the dynamic permeability model proposed by Johnson *et al.* (1987). Following the same procedure as in the isotropic case, we obtain a counterpart to the governing equations Eqs. (5) and (6) with coefficient matrices,

$$\mathbf{R} \equiv \begin{bmatrix} & 1/G \\ -G'\xi_1^2 + \rho - \dfrac{\rho_f^2}{\tilde{\rho}_1} & \end{bmatrix}, \tag{A7}$$

$$\mathbf{Q}_{XY} \equiv \begin{bmatrix} 1/G & \xi_1 & 0 \\ \xi_1 & \rho & \rho_f \\ 0 & \rho_f & \tilde{\rho}_3 \end{bmatrix}, \tag{A8}$$

$$\mathbf{Q}_{YX} \equiv \begin{bmatrix} \rho - \dfrac{\rho_f^2}{\tilde{\rho}_1} - \left(C_{11}^D - \dfrac{C_{13}^{D2}}{C_{33}^D}\right)\xi_1^2 & \xi_1 \dfrac{C_{13}^D}{C_{33}^D} & \xi_1\left(\alpha_1 - \alpha_3 \dfrac{C_{13}^D}{C_{33}^D} - \dfrac{\rho_f}{\tilde{\rho}_1}\right) \\ \xi_1 \dfrac{C_{13}^D}{C_{33}^D} & \dfrac{1}{C_{33}^D} & -\dfrac{\alpha_3}{C_{33}^D} \\ \xi_1\left(\alpha_1 - \alpha_3 \dfrac{C_{13}^D}{C_{33}^D} - \dfrac{\rho_f}{\tilde{\rho}_1}\right) & -\dfrac{\alpha_3}{C_{33}^D} & \dfrac{1}{M} + \dfrac{\alpha_3^2}{C_{33}^D} - \dfrac{1}{\tilde{\rho}_1}\xi_1^2 \end{bmatrix}. \tag{A9}$$

Using Eqs. (A7)–(A9), for a small fracture thickness h, formally identical simplified boundary conditions as in the isotropic case [Eqs. (46) and (52)] are obtained if the definitions of the characteristic fracture parameters are modified as follows:

$$\eta_T \equiv \frac{h}{G}, \tag{A10}$$

$$\eta_{N_D} \equiv \frac{h}{C_{33}^D}, \tag{A11}$$

$$\alpha \equiv \alpha_3, \tag{A12}$$

$$\hat{\kappa}(\omega) \equiv \frac{k_3(\omega)}{h}, \tag{A13}$$

$$\tilde{B} \equiv \frac{\alpha_3}{C_{33}^D} \Big/ \left(\frac{1}{M} + \frac{\alpha_3^2}{C_{33}^D}\right) = \alpha_3 \frac{M}{C_{33}^U}. \tag{A14}$$

Note that only the anisotropic material properties related to the 3 direction (fracture-normal direction) appear in these definitions, which indicates that the scattering of waves is not affected by the quantities related to the fracture-parallel directions (Specifically, permeability along the fracture). The fluid pressure dissipation factor Π is the same as the isotropic case if the direction of the slow P-wave propagation within the fracture is approximately in the fracture-normal direction. One important difference from the isotropic case, however, is that the normal and shear fracture compliances can take arbitrary values independent from each other.

APPENDIX B: THE DYNAMIC PERMEABILITY OF OPEN AND VERY PERMEABLE FRACTURES

For a highly permeable fracture or an open fracture in which fluid flow parallel to the fracture can be affected by the viscous friction along the fracture surfaces, the effective permeability of the layer representing a fracture in the frac-

ture parallel direction must be reduced. As shown in Appendix A, for a transversely isotropic fracture (a layer modeling the fracture is transversely isotropic), $\tilde{\mathbf{Q}}_{XY}$ contains only the fracture-normal permeability $k_3(\omega)$ and $\tilde{\mathbf{Q}}_{YX}$ contains only the fracture-parallel permeability $k_1(\omega)$. Therefore, for the isotropic fracture model discussed in the main body of this paper, the permeability needs to be allowed to be anisotropic.

In discussing the high-permeability case, we are concerned only with fracture-parallel permeability $k_1(\omega)$ in $\tilde{\mathbf{Q}}_{YX}$ because terms including $k_3(\omega)$ in the boundary conditions appear only as $h/k_3(\omega)$, which become negligibly small for small hs. If fracture-parallel fluid flow within the fracture is laminar and the flow on the fracture surfaces can be ignored because of the small permeability in the background, the maximum possible permeability for this fracture can be evaluated using Biot's results for the dynamic permeability of plane parallel flows (Biot, 1956b),

$$|k_1(\omega)| \leq |k_{\text{plane}(\omega)}| = \left| \frac{h^2}{4\theta^2}\left(1 - \frac{\tanh\,\theta}{\theta}\right)\right|, \tag{B1}$$

$$\theta \equiv \frac{h}{2}\sqrt{\frac{\rho_f \omega}{i\eta_f}}.$$

Therefore, the permeability for the flow in the fracture parallel direction is bounded by taking the limit of Eq. (B1) for $h \to \infty$

$$|k_1(\omega)| \leq \left| \frac{h^2}{4\theta^2}\right| = \frac{\eta_f}{\rho_f \omega}. \tag{B2}$$

Equation (B2) gives the maximum possible dynamic permeability of any fracture for a given fluid type. This limit can also be obtained directly from the momentum balance equation for an acoustic medium,

$$\nabla(-p_f) = -\omega^2 \rho_f \mathbf{U}. \tag{B3}$$

This equation can be rewritten as

$$\dot{\mathbf{U}} = \frac{i}{\omega\rho_f}\nabla(-p_f) \equiv \frac{k(\omega)}{\eta_f}\nabla(-p_f). \tag{B4}$$

Therefore, we identify the permeability as

$$k(\omega) = \frac{i\eta_f}{\omega\rho_f}, \tag{B5}$$

which is identical to Eq. (B2). The same expression can also be obtained by bringing the static permeability k_0 to infinity in the expression for in dynamic permeability given by Johnson *et al.* (1987),

$$k(\omega) = k_0 \Bigg/ \left(\sqrt{1 - i\frac{4}{n_J}\frac{\omega}{\omega_J}} - i\frac{\omega}{\omega_J}\right), \tag{B6}$$

where n_J is a finite parameter determined by the pore geometry (a value of 8 is recommended for common sandstones), and ω_J is the viscous-boundary characteristic frequency given by $\omega_J \equiv \eta_f/\rho_f F k_0 = \eta_f \phi/\rho_f \alpha_\infty k_0$, where F is the electrical formation factor and α_∞ is the high-frequency limit pore-space tortuosity, both of which approach unity for an open fracture.

Using Eq. (B2) and the definition in Eq. (4), we obtain

$$|\tilde{\rho}| \geq |\tilde{\rho}(k_0 \to \infty)| = \rho_f. \tag{B7}$$

This indicates that the magnitude of terms $h/\tilde{\rho}$ in $\tilde{\mathbf{Q}}_{YX}$ is bounded by a negligibly small value h/ρ_f for small h's. Therefore, permeability in the fracture parallel direction does not appear in the seismic boundary conditions for any static permeability values of the medium and does not affect the scattering of seismic waves. Conversely, permeability of a fracture in the fracture-parallel direction cannot be determined from measured seismic responses if the fracture thickness is much smaller than the wavelength of propagating seismic waves.

APPENDIX C: KENNETT'S REFLECTIVITY ALGORITHM APPLIED TO A SINGLE POROELASTIC LAYER

Pride *et al.* (2002) applied Kennett's reflectivity algorithm (Kennett, 1983) to piecewise-homogeneous layered poroelastic media. Exact expressions for the transmission and reflection coefficients of a single poroelastic layer representing a fracture can be obtained as a special case of the application.

Kennett method is based upon the following recursive relationships between the transmission and reflection coefficients for a group of n parallel interfaces and coefficients, for the remaining $n-1$ interfaces after the first interface in the series is removed:

$$\mathbf{T}^{(n)} = \mathbf{T}^{(n-1)}\mathbf{E}_n(\mathbf{I} - \mathbf{R}_n^- \mathbf{E}_n \mathbf{R}^{(n-1)}\mathbf{E}_n)^{-1}\mathbf{T}_n^+, \tag{C1}$$

$$\mathbf{R}^{(n)} = \mathbf{R}_n^+ + \mathbf{T}_n^- \mathbf{E}_n \mathbf{R}^{(n-1)}\mathbf{E}_n(\mathbf{I} - \mathbf{R}_n^- \mathbf{E}_n \mathbf{R}^{(n-1)}\mathbf{E}_n)^{-1}\mathbf{T}_n^+, \tag{C2}$$

where the transmission and reflection coefficient matrices for the removed interface are given as $\mathbf{T}_n$ and $\mathbf{R}_n$, respectively, with a sign in the superscript indicating the incident wave direction. $\mathbf{T}^{(n)}$, $\mathbf{T}^{(n-1)}$, $\mathbf{R}^{(n)}$, and $\mathbf{R}^{(n-1)}$ are for the n and $n-1$ interfaces, as indicated in the parentheses, and for incident waves propagating in the positive direction. $\mathbf{E}_n$ is the diagonal-phase advance matrix between the interfaces.

For the case of a single layer (two interfaces), no recursion is necessary to compute the transmission and reflection coefficients $\mathbf{T}$ and $\mathbf{R}$ for the whole system. By setting $\mathbf{T}^{(0)} = \mathbf{T}_0^+$, $\mathbf{R}^{(0)} = \mathbf{R}_0^+$, $\mathbf{T} = \mathbf{T}^{(1)}$, and $\mathbf{R} = \mathbf{R}^{(1)}$,

$$\mathbf{T} = \mathbf{T}_0^+ \mathbf{E}(\mathbf{I} - \mathbf{R}_1^- \mathbf{E}\mathbf{R}_0^+ \mathbf{E})^{-1}\mathbf{T}_1^+, \tag{C3}$$

$$\mathbf{R} = \mathbf{R}_1^+ + \mathbf{T}_1^- \mathbf{E}\mathbf{R}_0^+ \mathbf{E}(\mathbf{I} - \mathbf{R}_1^- \mathbf{E}\mathbf{R}_0^+ \mathbf{E})^{-1}\mathbf{T}_1^+. \tag{C4}$$

For in-plane wave propagation (fast and slow P waves and S waves with particle motions parallel to the plane of wave propagation), these matrices correspond to the transmission and reflection coefficient matrices in Eqs. (68) and (69). The phase advance matrix is $\mathbf{E} \equiv \text{diag}[e^{i\omega\xi_z^{Pf}h}\ e^{i\omega\xi_z^{Ps}h}\ e^{i\omega\xi_z^{S}h}]$. The transmission and reflection coefficient matrices for the individual interfaces are a function of material properties for both the background and the fracture layer, which results in very complex expressions for Eqs. (C3) and (C4) (albeit they are in closed form). These equations are evaluated numerically to obtain "correct solutions" in the example presented

in this paper. The interface scattering matrices can be computed, for example, using the equations presented by Pride *et al.* (2002).

Adams, J. T., and Dart, C. (**1998**). "The appearance of potential sealing faults on borehole images," in Faulting, Fault Sealing and Fluid Flow in Hydrocarbon Reservoirs, edited by G. Jones, Q. J. Fisher, and R. J. Knipe, Geol. Soc. Spec. Publ. **147**, 71–86.

Aydin, A. (**1978**). "Small faults formed as deformation bands in sandstone," Pure Appl. Geophys. **116**, 913–930.

Bakulin, A., and Molotkov, L. (**1997**). "Poroelastic medium with fractures as limiting case of stratified poroelastic medium with thin and soft Biot layers," *67th Annual International Meeting*, SEG, Expanded Abstracts, 1001–1004.

Bakulin, A., Grechka, V., and Tsvankin, I. (**2000**). "Estimation of fracture parameters from reflection seismic data. I. HTI model due to a single fracture set," Geophysics **65**, 1788–1802.

Berryman, J. G., and Wang, H. F. (**1995**). "The elastic coefficients of double-porosity models for fluid transport in jointed rock," J. Geophys. Res. **100**, 24611–24627.

Berryman, J. G., and Wang, H. F. (**2000**). "Elastic wave propagation and attenuation in a double-porosity dual-permeability medium," Int. J. Rock Mech. Min. Sci. **37**, 63–78.

Biot, M. A. (**1956a**). "Theory of elastic waves in a fluid-saturated porous solid. I. Low frequency range," J. Acoust. Soc. Am. **28**, 168–178.

Biot, M. A. (**1956b**). "Theory of elastic waves in a fluid-saturated porous solid. II. High frequency range," J. Acoust. Soc. Am. **28**, 179–191.

Brajanovski, M., Gurevich, B., and Schoenberg, M. (**2005**). "A model for P-wave attenuation and dispersion in a porous medium permeated by aligned fractures," Geophys. J. Int. **163**, 372–384.

Cheng, A. H.-D. (**1997**). "Material coefficients of anisotropic poroelasticity," Int. J. Rock Mech. Min. Sci. **34**(2), 199–205.

Coates, R. T., and Schoenberg, M. (**1995**). "Finite-difference modeling of faults and fractures," Geophysics **60**(5), 1514–1526.

Dutta, N. C., and Odé, H. (**1979a**). "Attenuation and dispersion of compressional waves in fluid-filled porous rocks with partial gas saturation (White Model)–I. Biot theory," Geophysics **44**, 1777–1788.

Dutta, N. C., and Odé, H. (**1979b**). "Attenuation and dispersion of compressional waves in fluid-filled porous rocks with partial gas saturation (White Model)–II. Results," Geophysics **44**, 1806–1812.

Gelinsky, S., and Shapiro, S. A. (**1997**). "Dynamic-equivalent medium approach for thinly layered saturated sediments," Geophys. J. Int. **128**, F1–F4.

Gurevich, B., Marschall, R., and Schapiro, S. A. (**1994**). "Effect of fluid flow on seismic reflections from a thin layer in a porous medium," J. Seism. Explor. **3**, 125–140.

Gurevich, B., Zyrianov, V. B., and Lopatnikov, S. L. (**1997**). "Seismic attenuation in finely layered porous rocks: Effects of fluid flow and scattering," Geophysics **62**(1), 319–324.

Gurevich, B., and Schoenberg, M. A. (**1999**). "Interface conditions for Biot's equations of poroelasticity," J. Acoust. Soc. Am. **105**(5), 2585–2589.

Haskell, N. A. (**1953**). "The dispersion of surface waves in multilayered media," Bull. Seismol. Soc. Am. **43**, 17–34.

Hsu, C.-J., and Schoenberg, M. A. (**1993**). "Acoustic waves through a simulated fractured medium," Geophysics **58**(7), 964–977.

Johnson, D. L. (**2001**). "Theory of frequency dependent acoustics in patchy-saturated porous media," J. Acoust. Soc. Am. **110**(2), 682–694.

Johnson, D. L., Koplik, J., and Dashen, R. (**1987**). "Theory of dynamic permeability and tortuosity in fluid-saturated porous media," J. Fluid Mech. **176**, 379–402.

Kennett, B. L. N. (**1983**). *Seismic Wave Propagation in Stratified Media* (Cambridge University Press, Cambridge).

Nakagawa, S., Nihei, K. T., and Myer, L. R. (**2002**). "Elastic wave propagation along a set of parallel fractures," Geophys. Res. Lett. **29**, 31-1–31-4.

Nihei, K. T., Weidong, Y., Myer, L. R., Cook, N. G. W., and Schoenberg, M. A. (**1999**). "Fracture channel waves," J. Geophys. Res. **104**(B3), 4769–4781.

Norris, A. N. (**1993**). "Low-frequency dispersion and attenuation in partially saturated rocks," J. Acoust. Soc. Am. **94**, 359–370.

Pride, S. R., Tromeur, E., and Berryman, J. G. (**2002**). "Biot slow-wave effects in stratified rock," Geophysics **67**(1), 271–281.

Pride, S. R. (**2003**). "Relationships between seismic and hydrological properties," in *Hydrogeophysics*, edited by Y. Rubin and S. Hubbard (Kluwer Academic, New York), pp. 1–31.

Pride, S. R., and Berryman, J. G. (**2003a**). "Linear dynamics of double-porosity and dual-permeability materials, I. Governing equations and acoustic attenuation," Phys. Rev. E **68**, 036603.

Pride, S. R., and Berryman, J. G. (**2003b**). "Linear dynamics of double-porosity and dual-permeability materials. II. Fluid transport equation," Phys. Rev. E **68**, 036604.

Pyrak-Nolte, L. J., and Cook, N. G. W. (**1987**). "Elastic interface waves along a fracture," Geophys. Res. Lett. **14**(11), 1107–1110.

Pyrak-Nolte, L. J., and Morris, J. P. (**2000**). "Single fractures under normal stress: The relation between fracture specific stiffness and fluid flow," Int. J. Rock Mech. Min. Sci. **37**, 245–262.

Pyrak-Nolte, L., Cook, N. G. W., and Myer, L. R. (**1990**). "Transmission of seismic waves across single natural fractures," J. Geophys. Res. **95**, 8516–8538.

Rokhlin, S. I., and Wang, Y. J. (**1991**). "Analysis of boundary conditions for elastic wave interaction with an interface between two solids," J. Acoust. Soc. Am. **89**(2), 503–515.

Schoenberg, M. A. (**1980**). "Elastic wave behavior across linear slip interfaces," J. Acoust. Soc. Am. **68**, 1516–1521.

Schoenberg, M. A., and Protazio, J. (**1992**). "Zoeppritz rationalized and generalized to anisotropy," J. Seism. Explor. **1**(2), 125–144.

Schoenberg, M. A., and Sayers, C. M. (**1995**). "Seismic anisotropy of fractured rock," Geophysics **60**, 204–211.

Shapiro, S. A., and Müller, T. M. (**1999**). "Seismic signatures of permeability in heterogeneous porous media," Geophysics **64**(1), 99–103.

Sibson, R. H. (**1977**). "Fault rock and fault mechanisms," J. Geol. Soc. (London) **133**, 191–213.

White, J. E., Mikhahaylova, N. G., and Lyakhovistsky, F. M. (**1975**). "Low-frequency seismic waves in fluid-saturated layered rocks," Izv., Acad. Sci., USSR, Phys. Solid Earth **11**, 654–659.